JCTC Journal of Chemical Theory and Computation

pubs.acs.org/JCTC Article

Constrained Nuclear-Electronic Orbital Transition State Theory Using Energy Surfaces with Nuclear Quantum Effects

Zehua Chen, Jingjing Zheng, Donald G. Truhlar, and Yang Yang*

Cite This: J. Chem. Theory Comput. 2025, 21, 590−604 Read Online

ACCESS | Metrics & More | Article Recommendations | Supporting Information

ABSTRACT: Hydrogen-atom transfer is crucial in a myriad of chemical and biological processes, yet the accurate and efficient description of hydrogen-atom transfer reactions and kinetic isotope effects remains challenging due to significant quantum effects on hydrogenic motion, especially tunneling and zero-point energy. In this paper, we combine transition state theory (TST) with the recently developed constrained nuclear-electronic orbital (CNEO) theory to propose a new transition state theory denoted CNEO−TST. We use CNEO−TST with CNEO density functional theory (CNEO−DFT) to predict reaction rate constants for two prototypical gas-phase hydrogen-atom transfer reactions and their deuterated isotopologic reactions. CNEO−TST is similar to conventional TST except that it employs constrained minimized energy surfaces to include zero-point energy and shallow tunneling effects in the effective potential. We find that the new theory predicts reaction rates quite accurately at room temperature. The effective potential surface must be generated by CNEO theory rather than by ordinary electronic structure theory, but because of the favorable computational scaling of CNEO−DFT, the cost is economical even for large systems. Our results show that dynamics calculations with this approach achieve accuracy comparable to variational TST with a semiclassical multidimensional tunneling transmission coefficient at and above room temperature. Therefore, CNEO−TST can be a useful tool for rate prediction, even for reactions involving highly quantal motion, such as many chemical and biochemical reactions involving transfers of hydrogen atoms, protons, or hydride ions.

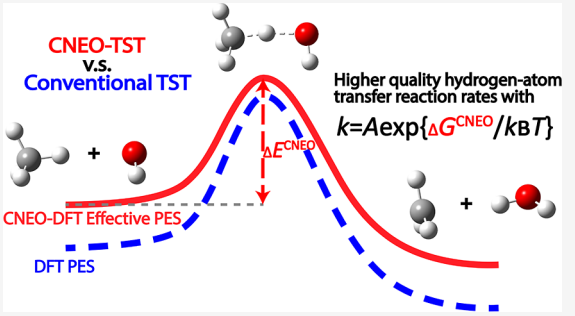

1. INTRODUCTION

Hydrogen-atom transfer (HAT) reactions involve the transfer of a hydrogen atom from one species to another, and they play a crucial role in many chemical and biological processes, including organic reactions and catalysis,[1−12] drug development,[13,14] and sustainable energy solutions.[15]

Theoretical predictions of the reaction rates of HAT reactions are challenging. A popular approach is transition state theory (TST).[16−19] Keys to the success of TST are variational determination of the transition state, accurate estimation of the free energy difference between the reactants and the transition state, and a reliable tunneling transmission coefficient. TST, in conventional or variational form, has been employed for qualitative, semiquantitative, and sometimes quantitative predictions of many chemical and biological reactions in both the gas phase[20−29] and the condensed phase.[30−35] However, the treatment of quantum mechanical zero-point energy (ZPE) and tunneling can make the attainment of accurate results more challenging for HAT reactions than for reactions that do not have large hydrogenic motion in the reaction coordinate.

A variety of methods have been developed to incorporate nuclear quantum effects into reaction rate constant calculations. These methods include quantum scattering theory[36−39] quantum wave packet dynamics,[40] quasiclassical trajectory methods,[41−45] path-integral[46−53] based reactive-flux methods,[54−56] instanton theory,[57,58] quantum transition state theory,[59,60] and variational transition state theory (VTST)[61,62] with semiclassical multidimensional tunneling (MT) transmission coefficients.[22,63,64] While these methods differ in terms of accuracy, efficiency, and scope of applicability, we will compare the new method presented in this article to CVT/SCT,[22] where CVT denotes the canonical variational theory form of VTST, and SCT denotes the small-curvature tunneling form of multidimensional tunneling, because this combination is a well-validated and widely applied method for practical calculations.[50,65−72]

In general, one distinguishes two kinds of TST, conventional TST (CTST) and VTST. Both forms of TST are dynamical theories that calculate the equilibrium flux through a dividing surface (the transition state) that separates reactants from products. The transition state—being a hypersurface—is

Received: November 11, 2024
Revised: December 20, 2024
Accepted: December 20, 2024
Published: January 7, 2025

missing one degree of freedom. In CTST, the transition structure passes through the saddle point between reactants and products and is missing the saddle point's imaginary-frequency normal mode.[16] In CVT, one defines a reaction path and a generalized free energy of activation as a function of location along the reaction path (the generalized free energy of activation is the free energy of activation calculated at any point on a reaction path, not just at a transition state), and the transition state is taken to pass through the reaction path at the point of maximum generalized free energy of activation and to be missing the degree of freedom corresponding to the reaction path. The reaction coordinate was originally defined in Cartesian coordinates,[73] but in most current work and the present work is taken as a curvilinear coordinate.[74,75] A key consequence of the TST rate being an equilibrium flux is that it can be calculated from partition functions (PFs).[76]

In the present article we make another distinction, namely the effective potential used in the PFs. In CTST and CVT, the potential energy surface is the usual Born−Oppenheimer potential energy surface.[77] Here we define a new kind of TST, denoted CNEO−TST, which takes the effective potential energy surface to be the surface that is obtained by using nuclear-electronic orbital ("NEO") theory[78] with a constraint[79] ("C") imposed on the expectation value of the quantum nuclear position. NEO treats not only the electrons but also key nuclei (here taken as the hydrogenic nuclei) quantum mechanically,[78,80,81] and CNEO constrains the expectation values of the quantal nuclei in order to obtain a coordinate-dependent energy that can serve as an effective potential energy surface.[79,82,83] The resulting effective potential energy surface is denoted as the constrained minimized energy surface (CMES)[84,85] or as the CNEO effective potential energy surface[79,82] and is interpreted as an addition of the quantum delocalization effect, which includes the ZPE, to the Born−Oppenheimer potential energy surface.

Direct dynamics, which is "the calculation of rates or other dynamical observables directly from electronic structure information, without the intermediacy of fitting the electronic energies in the form of a potential energy function,"[86] is the most convenient method for rate constant calculations. High-level electronic structure methods such as coupled cluster theory[87] with high-order excitations and an extended basis set can often give accurate potential energy surfaces (PESs), but their use for direct dynamics is usually prohibitively expensive. Density functional theory (DFT) is much more affordable and is the preferred method for direct dynamics on all but the smallest systems, especially since the development of modern functionals that predict relatively accurate reaction barrier heights for many cases.[88,89] The applications presented in this paper use Kohn−Sham density functional theory[90] for CVT/SCT and CNEO density functional theory[79,82] (CNEO−DFT) for CNEO−TST.

2. THEORY

We consider bimolecular reactions. The modifications to consider unimolecular reactions can be made similarly to the case of CTST.[62,91]

2.1. Conventional Transition State Theory. In CTST, a bimolecular chemical reaction rate constant k^{CTST} as a function of temperature T is calculated from the standard-state Gibbs free energy of activation $\Delta G_{\mathrm{act}}^{\ddagger,0}(T)$[92]

$$k^{\mathrm{CTST}} = \frac{k_{\mathrm{B}}T}{h}K^{0}(T)\exp\left[-\frac{\Delta G_{\mathrm{act}}^{\ddagger,0}(T)}{k_{\mathrm{B}}T}\right] \tag{1}$$

where k_{B} is the Boltzmann constant, h is the Planck constant

$$K^{0} = [c^{0}(T)]^{-1} = k_{\mathrm{B}}T/p^{0} = k_{\mathrm{B}}T/(1\ \mathrm{bar}) \tag{2}$$

and $\Delta G_{\mathrm{act}}^{\ddagger,0}$ is the difference between the standard-state Gibbs free energy of the transition state and that of reactants. It can be calculated as

$$\Delta G_{\mathrm{act}}^{\ddagger,0}(T) = -k_{\mathrm{B}}T\ln\left[\frac{c^{0}\Phi^{\ddagger}(T)}{\Phi^{\mathrm{R1}}(T)\Phi^{\mathrm{R2}}(T)}\right] \tag{3}$$

where Φ^{X} is the PF per volume of the transition state (X = ‡), reactant 1 (X = R1), or reactant 2 (X = R2). Notice that, throughout this whole article, we are taking the zero of energy for all PFs as the potential energy at the equilibrium geometry of the infinitely separated bimolecular reactants; thus, the barrier height is implicitly contained in $\Phi^{\ddagger}$.

For reactants and transition structures that each have only a single significant conformation, the PFs in eq 3 are assumed to be a product of a translational PF per unit volume (Φ_{trans}) and rotational (Q_{rot}), vibrational (Q_{vib}), and electronic (Q_{elec}) PFs

$$\Phi = \Phi_{\mathrm{trans}}(T)Q_{\mathrm{rot}}(T)Q_{\mathrm{vib}}(T)Q_{\mathrm{elec}}(T) \tag{4}$$

where the translational and rotational PFs are approximated classically, and the electronic part is calculated quantum mechanically from energy levels and electronic degeneracies

$$Q_{\mathrm{elec}}^{X} = \sum_{j} g_{j}\exp\left(-\frac{E_{\mathrm{gs}}^{X,\mathrm{elec}} + \Delta E_{\mathrm{ex},j}^{X,\mathrm{elec}}}{k_{\mathrm{B}}T}\right) \tag{5}$$

where the index j runs through all electronic levels with g_j being the degeneracy for the j-th level, $E_{\mathrm{gs}}^{X,\mathrm{elec}}$ is the equilibrium electronic energy of the ground electronic level of X, and $\Delta E_{\mathrm{ex},j}^{X,\mathrm{elec}}$ is the electronic excitation energy of level j. With our choice of the zero of energy, $E_{\mathrm{gs}}^{\mathrm{R1,elec}}$ and $E_{\mathrm{gs}}^{\mathrm{R2,elec}}$ are zero, and $E_{\mathrm{gs}}^{\ddagger,\mathrm{elec}}$ is the classical barrier height (often denoted as $V^{\ddagger}$).

The separable vibrational PF is calculated by quantum mechanical normal-mode analysis, which yields

$$Q_{\mathrm{vib}}^{X} = \prod_{i}\sum_{n_i=0}^{\infty}\exp\left[-\frac{\hbar\omega_i^{X}}{k_{\mathrm{B}}T}\left(n_i + \frac{1}{2}\right)\right] = \prod_{i}\frac{\exp(-\hbar\omega_i^{X}/2k_{\mathrm{B}}T)}{1 - \exp(-\hbar\omega_i^{X}/k_{\mathrm{B}}T)} \tag{6}$$

where ω_i^{X} is the frequency for the i-th normal mode (excluding the imaginary frequency associated with reaction-coordinate motion at the transition structure). The CTST and CVT/SCT calculations use the harmonic formula of eq 6 but with scaled harmonic frequencies;[93] with this scaling is called the quasiharmonic approximation.[64]

In cases where there is more than one important conformer due to torsional anharmonicity, the separability of rotation and vibration is no longer assumed, and the multistructural torsional anharmonicity model with a coupled torsional potential is used to calculate coupled conformational-rotational−vibrational PFs[94,95] (see Computational Details).

2.2. Canonical Variational Transition State Theory with Small-Curvature Tunneling (CVT/SCT). CVT/SCT is an extension to CTST that variationally optimizes the

https://doi.org/10.1021/acs.jctc.4c01521
J. Chem. Theory Comput. 2025, 21, 590−604

transition state location and includes multidimensional quantum effects on the reaction coordinate.[22,62,63] Quantum effects on the reaction coordinate include both tunneling at energies below the effective barrier top and nonclassical reflection at energies above it, but both effects are incorporated in a factor that is simply called the tunneling transmission coefficient. CVT with a multidimensional tunneling transmission coefficient that includes corner-cutting tunneling has been shown to yield HAT reaction rate constants that agree well with accurate quantum dynamics (which are practical only for the simplest reactions).[65,66] The success of CVT/MT depends on several important factors: a highly accurate PES, good choice of reaction coordinate (the reaction coordinate determines the dividing surface, since the latter is orthogonal to the former), an accurate treatment of vibrational anharmonicity, and a reliable way to estimate the tunneling contributions. In the present work, we use SCT as the choice of MT tunneling method. When used with high-quality potential energy surfaces (PESs), CVT/SCT often agrees well with experiment.[50,67−72]

Equating the reaction rate to the equilibrium flux through the transition state is only justified if the transition state is a dynamical bottleneck; otherwise, the rate constant is overestimated. Although the conventional transition state is located where the potential energy is a maximum along the minimum-energy reaction path, the location along the reaction path of the maximum in the free energy of activation may differ from the maximum of the potential energy. Because of the difference in these locations, free energies of activation obtained from a transition state passing through the highest potential energy along the reaction path will be lower than the true free energies of activation, and—if this were the only error—the rate constant would be overestimated. In CVT, this is ameliorated by replacing eq 1 by[61,62]

$$k^{\mathrm{CVT}} = \frac{k_{\mathrm{B}}T}{h}K^{0}(T)\exp\left[-\frac{\Delta G_{\mathrm{act}}^{\mathrm{CVTS},0}(T)}{k_{\mathrm{B}}T}\right] \tag{7}$$

where $\Delta G_{\mathrm{act}}^{\mathrm{CVTS},0}$ is the difference between the standard-state Gibbs free energy of the canonical variational transition state (CVTS) and that of reactants. In CVT, transition states are located by a search procedure carried out to find the maximum of the generalized free energy of activation $\Delta G_{\mathrm{act}}^{\mathrm{GT},0}$ as a function of the reaction coordinate s. We define s as the arc length along the curved minimum energy path (MEP) through isoinertial coordinates, which are coordinates mass-scaled to have the same mass μ in all directions, as explained elsewhere—see eq 2, 4, 8 in ref 19, and note that here we take μ = 1 amu. This search process requires the calculation of generalized normal modes[73−75] along the MEP. At 0 K, we have[96]

$$\begin{aligned}\Delta G_{\mathrm{act}}^{\mathrm{GT},0}|_{T=0} &= \Delta V_{\mathrm{a}}^{\mathrm{G}}(s)\\ &\equiv E_{\mathrm{gs}}^{\mathrm{GT,elec}}(s) + \varepsilon^{\mathrm{GT}}(s) - \varepsilon^{\mathrm{R1}} - \varepsilon^{\mathrm{R2}}\end{aligned} \tag{8}$$

where $\Delta V_{\mathrm{a}}^{\mathrm{G}}$ is the ground-state vibrationally adiabatic potential energy curve, $E_{\mathrm{gs}}^{\mathrm{GT,elec}}$ and $\varepsilon^{\mathrm{GT}}$ are respectively the potential energy and ZPE (excluding reaction-coordinate motion) along the MEP, and $\varepsilon^{\mathrm{R1}}$ and $\varepsilon^{\mathrm{R2}}$ are the ZPEs of the reactants. Note that $E_{\mathrm{gs}}^{\mathrm{GT,elec}}$ is called V_{MEP} when calculated by ordinary electronic structure theory (as is done in CTST and CVT/SCT), but eq 8 uses a notation designed for comparison to CNEO−TST.

In CVT/SCT, we evaluate the rate constant by[22,62,63]

$$k^{\mathrm{CVT/SCT}} = \kappa(T)\frac{k_{\mathrm{B}}T}{h}K^{0}(T)\exp\left[-\frac{\Delta G_{\mathrm{act}}^{\mathrm{CVTS},0}(T)}{k_{\mathrm{B}}T}\right] \tag{9}$$

where κ is the temperature-dependent tunneling transmission coefficient calculated in the SCT approximation. The effective barrier for tunneling in the SCT approximation is given by eq 8, and the effective mass for tunneling is a function of the curvature of the MEP.

2.3. Constrained Nuclear-Electronic Orbital Transition State Theory (CNEO−TST). There are three differences of CNEO−TST from CTST. First, the Born−Oppenheimer potential energy surfaces[77] are replaced by the CNEO effective potential energy surfaces.[79,82,84,85] This affects the potential along the reaction path, the vibrational frequencies (which are calculated from CNEO Hessians[83]), the rotational PFs (which are calculated using CNEO optimized geometries),[82] and the electronic PFs (which are calculated using CNEO energies).

Second, the zero-point energy is removed from eq 6 because it is effectively contained in the CNEO potential energy surfaces (this involves dropping 1/2 and replacing $\exp(-\hbar\omega_i^{\mathrm{X}}/2k_{\mathrm{B}}T)$ by unity in eq 6). Removing the zero-point energy from eq 6 prevents double counting because CNEO methods transform the classical potential energy along the reaction coordinate to a zero-point-energy-inclusive effective potential, allowing a classical treatment of dynamics on the effective potential.

There is also a third difference, namely that in the present implementation, the frequencies are not scaled. Anharmonicity corrections are not applied because with a quantum delocalized nuclear picture, the CNEO methods have been shown to have good accuracy for describing vibrational modes involving hydrogenic motions.

In the CNEO−TST framework, the product of vibrational and electronic PFs becomes

$$\begin{aligned}Q_{\mathrm{vib}}^{\mathrm{CNEO}}Q_{\mathrm{elec}}^{\mathrm{CNEO}} &= \prod_i \sum_{n_i=0}^{\infty}\exp\left(-\frac{n_i\hbar\omega_i}{k_{\mathrm{B}}T}\right)\\ &\quad\times\sum_j g_j\exp\left(-\frac{E_{\mathrm{gs}}^{\mathrm{CNEO}} + \Delta E_{\mathrm{ex},j}^{\mathrm{CNEO\text{-}elec}}}{k_{\mathrm{B}}T}\right)\\ &= \prod_i \frac{1}{1-\exp\left(-\frac{\hbar\omega_i}{k_{\mathrm{B}}T}\right)}\times\\ &\quad\sum_j g_j\exp\left(-\frac{E_{\mathrm{gs}}^{\mathrm{CNEO}} + \Delta E_{\mathrm{ex},j}^{\mathrm{CNEO\text{-}elec}}}{k_{\mathrm{B}}T}\right).\end{aligned} \tag{10}$$

If electronic excited states need to be considered, $\Delta E_{\mathrm{ex},j}^{\mathrm{CNEO\text{-}elec}}$ will be slightly different from Born−Oppenheimer excitation energies $\Delta E_{\mathrm{ex},j}^{\mathrm{elec}}$ because the electronic excitation energies $\Delta E_{\mathrm{ex},j}^{\mathrm{CNEO\text{-}elec}}$ in principle include some electron−nuclear coupling effects. However, we do not expect this difference to be significant because in almost all TST reaction rate calculations, populations in electronic excited states can be neglected except for small spin−orbit splittings, which are usually taken from experiment.

CNEO vibrational frequencies are not scaled because they are often significantly more accurate than the harmonic

https://doi.org/10.1021/acs.jctc.4c01521
J. Chem. Theory Comput. 2025, 21, 590−604

approximation for modes with strong hydrogenic character;[83,97−99] this is an important advantage of CNEO−TST.

CNEO−TST includes shallow tunneling. By "shallow tunneling" we refer to tunneling in which the tunneling energy is only slightly below the top of the effective barrier. Shallow tunneling can be understood in various ways, and one possible way is to make an analogy to path-integral-based theories because the delocalization of proton density across a barrier in CNEO is analogous to way that a Feynman-path-integral ring polymer[48] crosses a barrier top by slightly stretching the polymer and locating beads on both sides of the barrier. CNEO−TST does not include a tunneling transmission coefficient because shallow tunneling is contained in the effective potential. The success of the method without a tunneling transmission coefficient is a second important advantage of CNEO−TST when applied to problems with shallow tunneling.

2.4. Constrained Nuclear-Electronic Orbital Canonical Variational Transition State Theory (CNEO−CVT). In the CNEO framework, stationary geometries and reaction paths are obtained on temperature-independent, ZPE-inclusive effective PESs. As such, searches can still be carried out at each temperature to find the maximum generalized free energy of activation along the MEP, and this is called CNEO−CVT. We will see below, for two reactions, that CNEO−CVT does not offer a significant improvement over CNEO−TST. This can be a third important advantage of CNEO−TST.

3. RESULTS AND DISCUSSION

3.1. D + H_2 → DH + H. We first investigate the simplest hydrogen transfer reaction D + H_2 → DH + H, which was one of the first reactions studied with CVT and a corner-cutting tunneling transmission coefficient.[100] Figure 1 compares rate constants obtained by experiment[101−103] with those calculated in the present work.

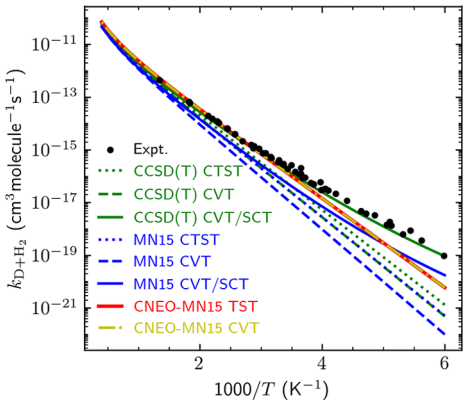

Figure 1. D + H_2 → DH + H rate constants as functions of reciprocal temperature. Experimental results are from refs 101−103.

With CTST, the Minnesota functional MN15[89] performs similarly to coupled cluster theory with single and double excitations and quasiperturbative treatment of connected triple excitations [CCSD(T)],[104] and both underestimate the reaction rate constants, with especially severe deviations at and below room temperature. The reason for these poor results at low T is the omission of tunneling in CTST. This underestimation is even more pronounced after the CVT optimization of the transition state location is performed for both CCSD(T) or MN15, which shows that optimization of the location of the transition state has an important effect.

When tunneling effects are included via CVT/SCT, both CCSD(T) and MN15 give significantly more accurate results. These results are consistent with many past studies showing that CVT with a corner-cutting tunneling transmission coefficient can accurately predict reaction rate constants for a variety of gas-phase reactions,[65,66,100] exhibiting excellent agreement with experiments. However, although MN15 has nearly the same potential energy barrier height as CCSD(T) [9.84 kcal/mol for MN15/MG3S and 9.77 kcal/mol for CCSD(T)/aug-cc-pVTZ], it is less accurate than CCSD(T) when dynamics is treated by CVT/SCT. The reason is that, although MN15 predicts a similar PES to CCSD(T) along the minimum-energy reaction path, as shown in Figure 2, the

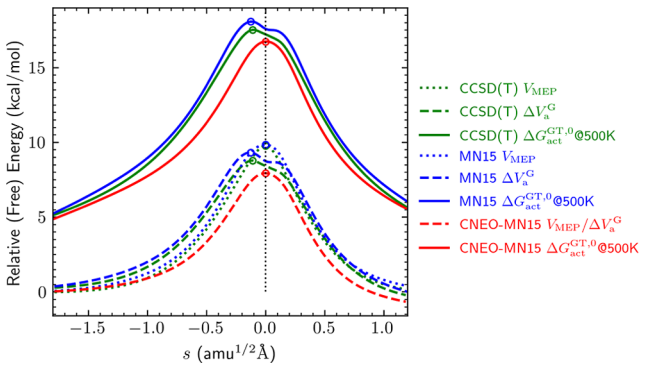

Figure 2. Potential energies (V^{MEP}, dotted lines), vibrationally adiabatic ground-state energies (ΔV_a^G, eq 8, dashed lines), and generalized free energies of activation at 500 K ($\Delta G_{act}^{GT,0}$, solid lines) for D + H_2 → DH + H by different methods along respective MEPs. The origin (s = 0 amu$^{1/2}$ Å, at which there is a vertical dotted line) of the reaction coordinate corresponds to the saddle point in each theory. The locations of the highest points for all curves are marked with circles. The V^{MEP} and ΔV_a^G curves by CNEO-MN15are the same because the vibrational ZPE is already incorporated in the CNEO total energy.

approximately scaled frequencies for those normal modes orthogonal to the reaction coordinate are slightly overestimated by MN15, which leads to a higher ZPE for the transition state and thus higher free energy barriers and lower reaction rate constants. This result shows that not only accurate potential energy barriers but also reliable vibrational frequencies are critical for the accurate prediction of reaction rate constants.

Because CNEO coupled cluster theory is yet to be developed, our CNEO results are currently limited to DFT. Without variationally optimizing the transition state location, CNEO−TST employing the CNEO−MN15 effective PES significantly outperforms CTST employing the MN15 Born−Oppenheimer PES. Overall, it yields highly accurate results near and above room temperature ($1000/T \lesssim 3.4$), although it begins to underestimate the rate constants at lower temperatures.

CNEO−CVT yields very similar results to CNEO−TST (Figure 1) for this reaction. This can be rationalized from the finding that the CNEO−CVT-MN15 transition state is close to the maximum of the CNEO-MN15 effective PES along the MEP, even at a temperature as high as 500 K (see Figure 2.) In contrast, there is a significant difference between the transition state locations in CTST and CVT, resulting in large differences

https://doi.org/10.1021/acs.jctc.4c01521
J. Chem. Theory Comput. 2025, 21, 590−604

in the predicted rates. This contrast is found because CNEO−TST calculates the flux through a transition state that has a maximum sum of the electronic energy and the nuclear zero-point energy. CVT also accounts for the effect of vibrationally excited states on the location of the variational transition state; however, this does not lead to a large effect on the location of the variational transition state in the case under consideration. Therefore, the key issue at the temperatures under consideration here is the accurate treatment of the vibrational ground state. When the vibrational ground state is the dominantly populated state, CVT locates the dynamical bottleneck away from the saddle point of the potential energy surface. This displacement occurs because, while the saddle point represents the highest-potential-energy point along the reaction path, the actual rate-determining configuration exists where the combined potential and zero-point energy reaches its maximum. Since the effective potential surface of CNEO is already a measure of the potential energy plus the zero-point energy, the dynamical bottleneck can equally well be found by locating the point on the reaction path with the highest value of the CNEO effective potential. As TST calculations are simpler than CVT, the good agreement of CNEO−TST and CNEO−CVT, if also observed for complex reactions, could be a significant computational advantage.

The good performance of CNEO−TST relative to CTST has two causes. (1) It is known from previous work[96] that the maximum of ΔV_a^G is often located close to the maximum of the generalized free energy of activation, even at finite temperatures and even when the maximum is not at $s = 0$. CNEO inherently incorporates zero-point energies in its effective PES; consequently, its effective PES along the reaction path aligns more closely with the Born−Oppenheimer ΔV_a^G than with the Born−Oppenheimer PES, and therefore it is less necessary to variationally optimize the transition state location with CNEO−TST than with CTST. (2) In the vicinity of the transition structure geometry, CNEO predicts a slightly more delocalized nuclear density, lowering the ZPE contribution to the effective potential barrier. This may be interpreted as a manifestation of shallow tunneling effects.

CNEO-TST-MN15 is also noticeably more accurate than CVT/SCT-MN15 near room temperature, apparently due to the already-discussed apparent inaccuracy of the MN15 vibrational ZPEs for the normal modes transverse to the reaction path. However, at temperatures below 250 K, the CNEO−TST method falls short of capturing the important deep tunneling effects, which require an even more delocalized nuclear density distribution. As a result, CNEO−TST underestimates the rate constant at the lowest temperatures.

3.2. H + D_2 → HD + D. We next investigated the isotopologic reaction H + D_2 → HD + D, in which a deuterium atom rather than a protium atom is transferred. The experimental[102,105,106] and computational results are presented in Figure 3. The performance of each method is very similar to the hydrogen-atom-transfer case, except that since D has a weaker tunneling contribution, the underestimation by the methods without tunneling transmission coefficients is less significant. It is encouraging that results from CNEO−TST calculations agree well with experiment and with CVT/SCT for both isotopologues.

3.3. CH_4 + OH → CH_3 + H_2O. Next, we explore the more complex reaction CH_4 + OH → CH_3 + H_2O. Figure 4 presents the computed and experimental rate constants. The latter are

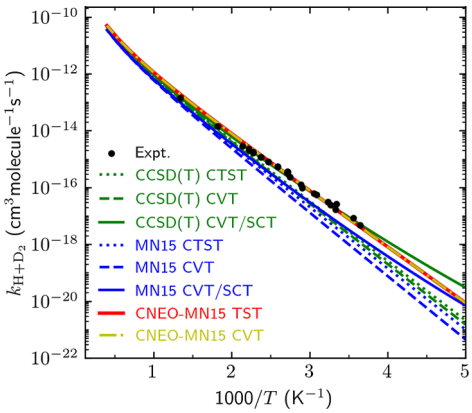

Figure 3. H + D_2 → HD + D rate constants as functions of reciprocal temperature. Experimental results are from refs 102 and 105.

from the fit by Srinivasan et al.,[107] which is $k = 1.66 \times 10^{-18} T^{2.182} \exp(-1231\ K/T)$ cm^3 $molecule^{-1}$ s^{-1}.

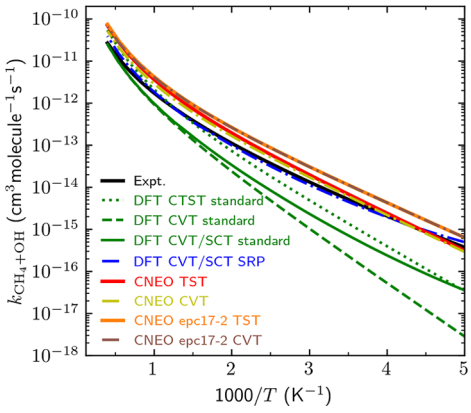

Figure 4. CH_4 + OH → CH_3 + H_2O rate constants as functions of reciprocal temperature. The electronic density functional is M08-HX in all cases. The results labeled "standard" were calculated with the standard vibrational scale factor (0.973), and those labeled "SRP" were calculated with a specific reaction parameter for the vibrational scale factor.

For this reaction, we chose the M08-HX functional[88] with the MG3S basis set,[108] which provides a potential energy barrier of 6.46 kcal/mol. This value is in good agreement with the reference barrier of 6.50 kcal/mol (without spin−orbit coupling) from the HTBH38/08 data set,[109,110] making it the most accurate among popular functionals (see data from ref 111). Furthermore, the reaction barrier is close to that obtained from UCCSD(T)-F12a/aug-cc-pVTZ calculations (6.29 kcal/mol).[112]

With the standard scale factor 0.973,[93] CTST with M08-HX significantly underestimates the reaction rate constants at and below room temperature. The CVT rate constant is even lower. However, CVT/SCT leads to great improvement. These performances are similar to those observed in the D + H_2 → DH + H case. The underlying reason remains that the CVT optimization decreases the predicted rate constants by identifying the highest free energy barrier along the MEP, while the tunneling contribution increases the rate constants. In this case, these two effects almost cancel each other such that CTST agrees reasonably well with CVT/SCT. However, the CVT/SCT-M08-HX results with the standard scale factor

https://doi.org/10.1021/acs.jctc.4c01521
J. Chem. Theory Comput. 2025, 21, 590−604

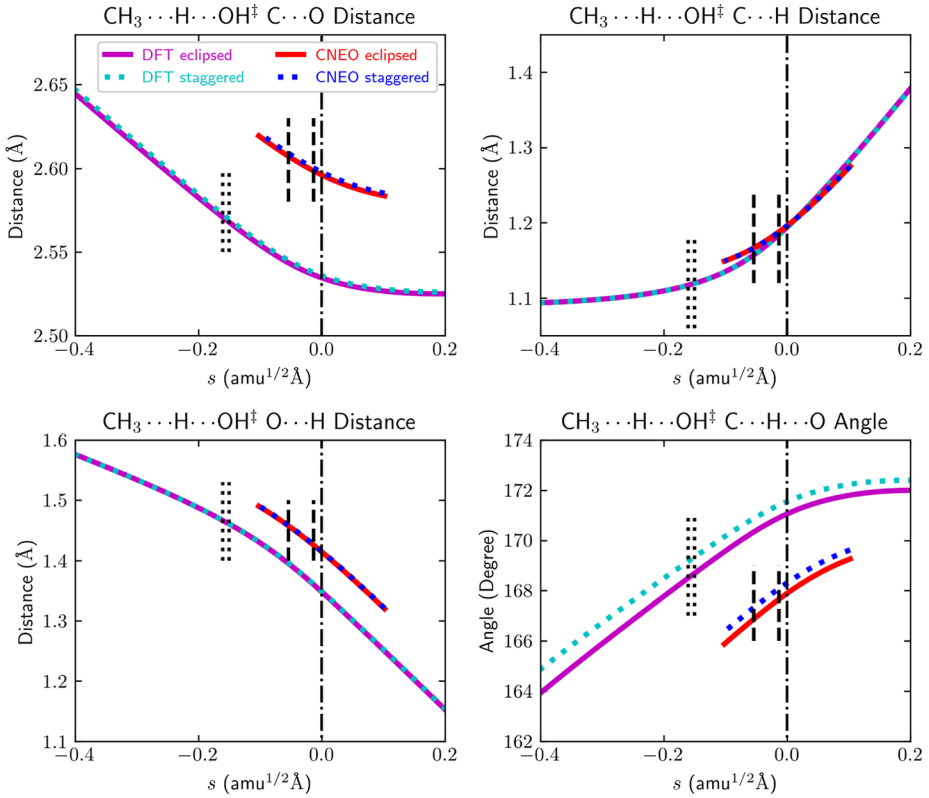

Figure 5. C···O distance, the bond-forming O···H distance, the bond-breaking C···H distance, and the C···H···O bond angle along the respective MEPs of the CVT and CNEO−CVT calculations on the CH_4 + OH → CH_3 + H_2O reaction. In each calculation, we use dashed curves for the staggered conformer and solid curves for the eclipsed conformer. The two dotted vertical lines at negative s denote the variationally optimized CVT geometries for the two conformers at 300 K with conventional DFT and SRP scale factors. The two dashed vertical lines denote the variationally optimized CVT geometries obtained using CNEO−DFT. It can be seen that CNEO−DFT produces CVT geometries that are very close to their transition structures, and other than the C···H distance, the CVT optimization always drives the conventional DFT geometry in the direction of the s = 0 CNEO geometry, that is, the DFT CVT optimized geometry always gets more similar to the CNEO transition structure geometry.

are unsatisfactory. The issue lies again in the vibrational frequencies. Although M08-HX accurately predicts the classical barrier height, its standard scale factor leads to an overestimated barrier on the vibrationally adiabatic ground-state potential energy curve. This discrepancy is a known limitation of using standard scale factors at transition structures,[113] and it is perhaps not surprising since the standard scale factors were determined for stable molecules that tend to have less anharmonicity than transition structures.

Following the procedure that has been used in several previous papers,[27,72,113−121] we used hybrid degeneracy-corrected second-order simple perturbation theory[122−125] (HDCPT2) to determine specific-reaction-parametrized (SRP) scale factors for each of the two possible transition structure conformers of this specific reaction (see Computational Details) while retaining standard scale factors for reactants. The resulting scale factors are smaller than the standard scale factor and result in a lower barrier on the ΔV_a^G curve and thus higher rate constants. As shown in Figure 4, the M08-HX CVT/SCT prediction is significantly improved when the SRP scale factors are applied to the transition structure conformers.

With the same M08-HX functional, the overall accuracy of CNEO−TST, which does not need scaling, is again notably better than that of CTST with the standard scale factor. The good performance can be partially rationalized from the transition structure geometries. We find that the geometry corresponding to the maximum potential on the CNEO effective potential energy profile agrees better with geometry at the maximum of the Born−Oppenheimer ΔV_a^G curve than with the geometry at the maximum of the V_{MEP} curve. This is illustrated in Figure 5, which shows that—other than the C···H distance—the CVT optimization always drives the conventional DFT geometry in the direction of the s = 0 CNEO geometry, that is, the DFT CVT optimized geometry always gets more similar to the CNEO transition structure geometry.

The CNEO−TST rate constants have optimal accuracy near room temperature due to the incorporation of ZPE and shallow tunneling effects. At lower temperatures, where deep tunneling effects become more pronounced, CNEO−TST again starts to underestimate the rate constants. At higher temperatures, the CNEO−TST curve exhibits a parallel behavior to that of CVT/SCT with the SRP scale factor for the transition structure, albeit with an overestimation by roughly a factor of 2.

Several factors may contribute to the CNEO−TST overestimation. First, it is known that TST without optimizing the transition state location may overestimate rate constants at higher temperatures due to the neglect of recrossing effects.[65] Second, the CMES employed here corresponds to a quantum calculation only for the ground vibrational state, so the CNEO effective PES is a low-temperature effective PES and, in an ideal scenario, a zero-temperature effective PES if electron−nuclear correlation effects could be fully accounted for.[84,126,127] The more approximate nature of the vibrational treatment for excited vibrational states may be a cause of larger error at high

https://doi.org/10.1021/acs.jctc.4c01521
J. Chem. Theory Comput. 2025, 21, 590−604

temperature. Third, due to the DFT treatment, inevitable errors may persist in both electronic and nuclear energies, which are concealed within the total CNEO energy in all calculations. Evaluating the magnitudes of these errors requires systematic benchmark work, and further investigations of these factors are beyond the scope of the present paper.

As a preliminary test of the neglect of electron−proton correlation, we have performed calculations with the electron−proton correlation functional epc17−2,[128] and the results are also presented in Figure 4. With the epc17−2 functional, CNEO-TST provides rate constants similar to those without electron−proton correlation, although some of the details, such as the quantitative accuracy of the zero-point energies, do change.[128] However, since the epc17−2 functional is approximate, it would be premature to conclude that the neglect of electron−proton correlation is not a possible source of error, and this remains an area for future study.[129]

3.4. CD_4 + OH → CD_3 + HDO. Finally, we performed calculations on the deuterium-atom-transfer reaction CD_4 + OH → CD_3 + HDO; the experimental[130,131] and calculated rate constants are presented in Figure 6.

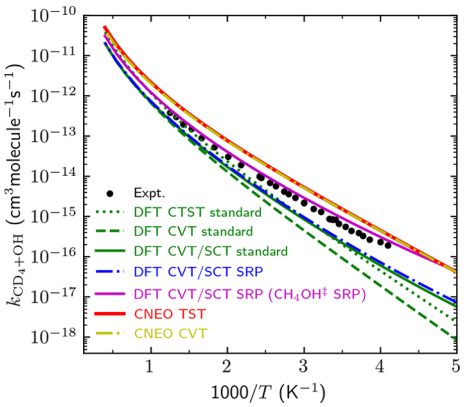

Figure 6. CD_4 + OH → CD_3 + HDO rate constants as functions of reciprocal temperature. The underlying electronic functionals are all M08-HX. DFT results labeled with "standard" indicate the use of the standard scale factor 0.973, while "SRP" indicates the use of specific-reaction-parametrized scale factors from the HDCPT2 calculation of $CD_4OH^‡$. The curve labeled with "SRP ($CH_4OH^‡$ SRP)" utilizes the SRP scale factors obtained from the HDCPT2 calculation of $CH_4OH^‡$ for the transition structure of CD_4^+OH reaction. Experimental results are from refs 130 and 131.

Due to the larger nuclear mass and smaller tunneling effects in the deuterium case, the CTST calculation with the standard scale factor performs slightly better than in the protium case, although the rate constant is still underestimated. The CVT/SCT calculations underestimate the rate. To explore the impact of SRP scale factors, we also conducted HDCPT2 calculations for the deuterated transition structures. However, the obtained SRP scale factors for the transition structure conformers are much larger than those in the case of $CH_4OH^‡$, resulting in SRP-scale-factor CVT/SCT results similar to standard-scale-factor CVT/SCT results. It is unclear why the SRP procedure is insufficient for good results in this case. Curiously, if we apply the SRP scale factors of $CH_4OH^‡$ to $CD_4OH^‡$, the SRP CVT/SCT rate constants agree much better with experimental results; this is presumably due to cancellation of errors, but it does illustrate again the uncertainties that can be caused by anharmonicity.

CNEO−TST, which does not use any scaling, exhibits roughly the same level of overestimation (about a factor of 2−3) as observed in the protium-atom-transfer reaction, presumably with reasons analogous to the hydrogen-atom-transfer case. As with the protium case, we again observe similarities in transition structure geometries between CNEO−TST and conventional CVT/SCT (Figure 7), although at temperatures at and below room temperature, CNEO−TST has better agreement than CVT/SCT with the experimental rate constants.

For this more complex reaction, CNEO−CVT again yields very similar results to CNEO−TST (Figure 6). The rationale behind this behavior is the same as already presented above. Consequently, within the CNEO framework, good results are obtained without a tunneling transmission coefficient and without optimizing the transition state location.

The kinetic isotope effect (KIE) for the CH_4 and CD_4 reactions with OH is presented in Figure 8. The experimental curve is almost linear on the Arrhenius plot.[131] CTST with the standard scale factor performs exceptionally well, yielding the most accurate KIE predictions. The good agreement results from predicting similar underestimates for protium and deuterium transfer. CVT/SCT with the standard scale factor has a more physically correct picture but underestimates the KIE. With the SRP scale factor, the KIE is significantly increased and becomes overestimated, and only with the SRP scale factor transferred from $CH_4OH^‡$ to $CD_4OH^‡$ can the KIE be reasonably described. In contrast, without any scaling, CNEO−TST gives a prediction that is reasonably close to the experimental results although with a slight underestimation. This underestimation is because CNEO gives a slightly larger error for deuterium, which is heavier and thus behaves more classically than hydrogen.

It is fortuitous that CTST with standard scale factors performs well on the KIE. As seen from the rate constant results, CTST with standard scale factors underestimates the rate constants for both CH_4 and CD_4, and there are several sources of errors such as the missing variational optimization of the transition state location, the omission of a tunneling transmission coefficient, and the error in the zero-point energy due to using standard scale factors. These errors happen to accumulate similarly enough for CH_4 and CD_4 that the KIE is reasonably accurate. This error cancellation is not guaranteed to happen for all systems, and ample previous work[132−139] shows that we cannot rely on CTST for accurate predictions of KIEs. Although CNEO−TST may still face challenges in the low-temperature deep tunneling regime, it has high promise as an inexpensive and black-box method for applications to more complex chemical and biological systems at room temperature.

3.5. General Discussion. The leading contributions to reaction kinetics from vibrational anharmonicity are of three types: anharmonic ZPE due mainly to high-frequency modes, multiple-structure anharmonicity due to multiple conformers, and torsional potential anharmonicity. For polyatomic reactions, the ZPE is large, and therefore a small change in the ZPE can have a large effect on the predicted rate constants. For inclusion of anharmonic ZPE in CTST and CVT/SCT, a practical method is harmonic analysis with reactant frequencies scaled by a factor optimized against stable molecules[93] and with scale factors for transition structures determined by HDCPT2.[113] Although HDCPT2 can be problematic for large-amplitude vibrations, the ZPE is dominated by high-frequency modes for which it should be acceptable. However, this issue

https://doi.org/10.1021/acs.jctc.4c01521
J. Chem. Theory Comput. 2025, 21, 590−604

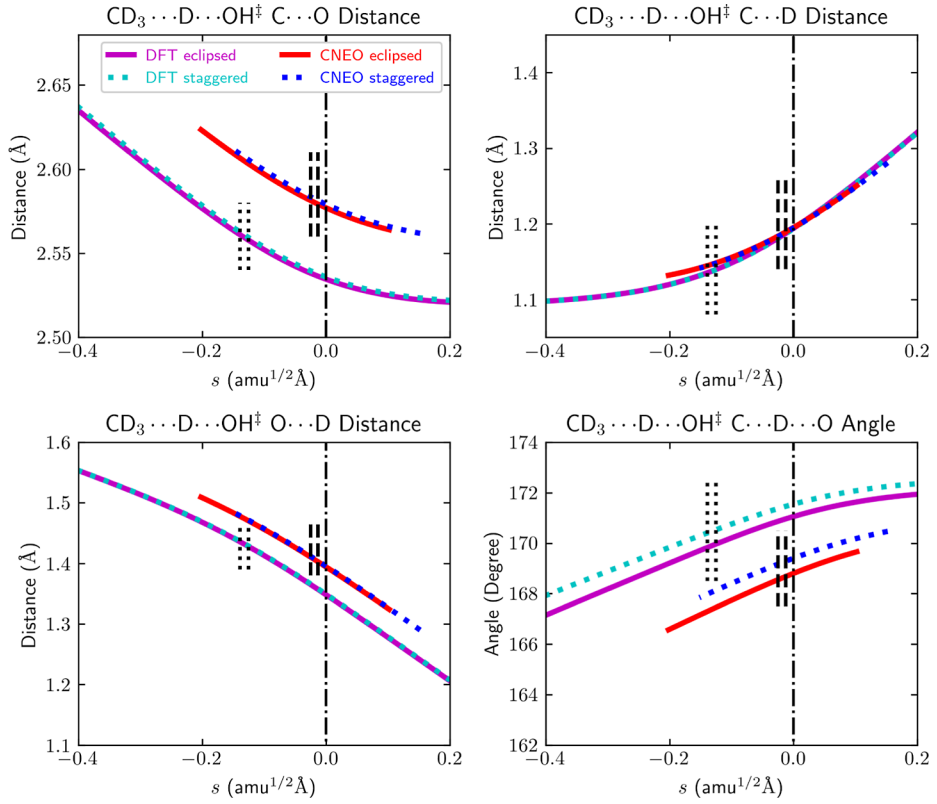

Figure 7. Same as Figure 5 except for CD_4 + OH → CD_3 + HDO reaction.

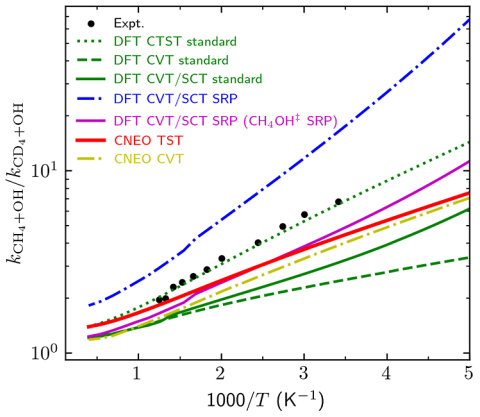

Figure 8. Kinetic isotope effects between CH_4^+OH and CD_4^+OH. The underlying electronic functionals are all M08-HX. DFT results labeled with "standard" indicate the use of the standard scale factor 0.973, while "SRP" indicates the use of specific-reaction-parametrized scale factors from the HDCPT2 calculation of $CD_4OH^‡$. The curve labeled with "SRP ($CH_4OH^‡$ SRP)" utilizes the SRP scale factors obtained from the HDCPT2 calculation of $CH_4OH^‡$ for the transition structure of CD_4^+OH reaction. Experimental results are from ref 131.

does not arise in the present CNEO−TST calculations because the ZPE is included via the CNEO−DFT calculation, which does not make the harmonic approximation.

CVT requires one to choose a reaction path, and the MEP in isoinertial (i.e., mass-scaled) coordinates[73,140] is often sufficiently accurate for calculating overbarrier contributions to the rates. However, care needs to be taken to ensure that the MEP is calculated over a long enough path to include the variational transition state and that an accurate enough generalized normal-mode analysis is made, which is complicated by the usual need to use a curvilinear-coordinate[74,75] analysis. Furthermore, an accurate estimate of tunneling contributions usually requires an even wider range of the reaction path. Thus, the computational procedure of CVT/MT involves construction of a reaction path and generalized-normal-mode[61] PFs over a range wide enough to include the variational transition state and the portion of the barrier through which appreciable tunneling occurs. Moreover, to obtain accurate results with highly anharmonic transition structures, one often needs to calculate SRP scale factors,[113] which adds further complexity to the process. In contrast, even without the CVT optimization of the transition state location and without a semiclassical tunneling coefficient, the new CNEO−TST method can accurately predict the HAT rate constants at room temperature, although the results may be slightly worse at higher and lower temperatures.

This performance of CNEO−TST is especially striking when compared to CTST. Although CNEO−TST may still face challenges in the low-temperature deep tunneling regime, it has high promise as an inexpensive and black-box method for applications to more complex chemical and biological systems at room temperature.

Further insight into the shallow tunneling is provided by calculating the temperature-dependent Arrhenius energy of activation E_a for the CH_4 + OH reaction by

$$E_a = -R\mathrm{d}\ln k/\mathrm{d}(1/T) \tag{11}$$

where R is the gas constant. Recall the Tolman interpretation of E_a, namely that it equals the average energy of reacting pairs of reagents minus the average energy of all pairs of reagents.[141,142] The activation energies computed by various methods are given in Table 1, and we focus on two temperature ranges, from 450 to 275 K, where we might see

https://doi.org/10.1021/acs.jctc.4c01521
J. Chem. Theory Comput. 2025, 21, 590−604

Table 1. Arrhenius Activation Energy E_a (in kcal/mol) of the CH_4 + OH Reaction

T (K)	expt	DFT CTST standard	DFT CVT standard	DFT CVT/SCT standard	DFT CVT/SCT SRP	CNEO TST	CNEO CVT	CNEO epc17−2 TST	CNEO epc17−2 CVT
1000	6.8	8.2	8.5	8.3	7.5	7.3	7.1	7.0	6.8
850	6.1	7.5	7.9	7.5	6.7	6.6	6.4	6.3	6.1
700	5.5	6.7	7.3	6.5	6.0	5.8	5.7	5.5	5.5
550	4.8	6.0	6.7	6.1	5.2	5.1	5.0	4.8	4.8
450	4.4	5.5	6.3	5.6	4.6	4.7	4.7	4.4	4.4
400	4.2	5.3	6.2	5.3	4.3	4.5	4.4	4.2	4.2
350	4.0	5.2	6.1	5.0	4.0	4.3	4.3	4.1	4.1
300	3.7	5.0	5.9	4.6	3.6	4.2	4.1	3.9	3.9
275	3.6	5.0	5.9	4.4	3.4	4.1	4.1	3.9	3.9
250	3.5	4.9	5.8	4.1	3.1	4.1	4.0	3.8	3.8
225	3.4	4.9	5.8	3.8	2.8	4.1	4.0	3.8	3.8
200	3.3	4.9	5.8	3.4	2.3	4.0	4.0	3.8	3.8

the most sensitivity to shallow tunneling, and 275−200 K, where we might expect to see the most sensitivity to deep tunneling. We also focus on comparing CVT, which is the best calculation without tunneling, to CVT/SCT and CNEO−TST, which include tunneling. The CVT E_a drops 0.4 kcal/mol in the first range and 0.1 kcal/mol in the second, whereas the CVT/SCT E_a drops 1.2 kcal/mol in the first range and 1.0 kcal/mol in the second; the faster drop in both temperature ranges when tunneling is included indicates significant shallow tunneling and significant deep tunneling. The CNEO E_a drops 0.6 kcal/mol in the first region, which a greater drop than CVT, possibly indicating some nuclear quantum effects, but only 0.1 kcal/mol in the second range, the same as CVT, indicating little or no deep tunneling. An alternative way to see the shallow tunneling is to compare the barrier in CVT with the effective barrier in CNEO TST; we find 5.8 kcal/mol for the former and 4.0 kcal/mol for the latter. This shows the effect of tunneling and is consistent with our interpretation above, and it illustrates how proton delocalization can enhance Arrhenius curvature at room temperature. If we consider the broader temperature range from 1000 to 275 K, the experimental E_a drops by 3.2 kcal/mol, and the CNEO one decreases by 2.9−3.1 kcal/mol, in excellent agreement with experiment.

The present paper is mainly concerned with showing the ability of the new method to include quantum nuclear delocalization in dynamics. However, we also wish to stress the strength for practical applications of combining CNEO-TST with DFT. Although wave function theories can achieve systematic improvement, DFT is known for its balanced efficiency and accuracy. The computational cost of CNEO−DFT is essentially the same as conventional DFT, with only a modest computational increase (typically less than 20%).[98,99] This is because CNEO theory exploits the physical picture that nuclei are relatively localized and can be treated as distinguishable particles, which ensures that the primary computational cost remains in the electronic part. Consequently, with a careful choice of density functionals, CNEO−TST is highly promising for obtaining accurate rate constants for large and complicated systems where DFT would be the only affordable structural method capable of high accuracy.

We note that for condensed-phase reactions, solvent effects can be included in two ways. First, solvent molecules can be added explicitly, and reaction rates can be calculated by combining CNEO with ensemble-averaged variational transition state theory.[68] Second, solvent effects can be included implicitly using models such as SMD,[143] SM12,[144] or the polarized continuum method,[145] where the potential energy function is replaced by the free energy surface derived from the liquid-phase potential of mean force.[34] For example, CNEO has already been combined with QM/MM[146] and implicit solvent models,[147] so extending the present approach to study condensed-phase reactions is straightforward.

4. SUMMARY

In this study, we defined a new version of transition state theory by combining the constrained nuclear-electronic orbital framework with conventional transition state theory to make CNEO−TST, and we applied the new theory to compute hydrogen-atom-transfer reaction rate constants with direct incorporation of nuclear quantum effects. CNEO−TST differs from conventional rate theory by using constrained minimized energy surfaces to include ZPEs and shallow tunneling effects in the effective potential. By using constrained nuclear-electronic orbital density functional theory to generate the surfaces, we showed that CNEO−TST can give accurate hydrogen-transfer rate constants for two protium-transfer reactions and two deuterium-transfer reactions at a very economical computational cost. CNEO−TST gives results similar in quality to canonical variational theory with a small-curvature tunneling transmission coefficient except in the deep tunneling regime. Particularly noteworthy in the present application to protium and deuterium transfer is the good accuracy of CNEO−TST at room temperature, making it a promising approach for future applications to complex chemical and biochemical reactions.

5. COMPUTATIONAL DETAILS

5.1. Electronic Structure. The CCSD(T) calculations used the aug-cc-pVTZ[148] basis set. CCSD(T) gradients and Hessian matrices were computed by numerical differentiation of energies. The CNEO−DFT calculations used the same electronic density functional choices and electronic basis sets as used for DFT. For DFT calculations, we used different functionals for different reactions with the choice based on prior benchmark data.[111] The MN15 functional[89] was used for $D + H_2 \rightarrow DH + H$ and $H + D_2 \rightarrow HD + D$, and the M08-HX functional[88] was used for $CH_4 + OH \rightarrow CH_3 + H_2O$ and $CD_4 + OH \rightarrow CD_3 + HDO$. These functionals were carefully chosen as they exhibit small deviations of their barrier heights relative to reference values [CCSD(T) results or estimated values from experiments]. In contrast, some general-purpose

https://doi.org/10.1021/acs.jctc.4c01521
J. Chem. Theory Comput. 2025, 21, 590−604

functionals such as B3LYP (which was suggested for discussion by a reviewer) would introduce significant errors in the electronic structure of transition structures and lead to rate predictions that are incorrect by orders of magnitude. The MG3S electronic basis set[108] was employed for DFT calculations; this is equivalent to the 6-311+G(2df,2p) basis set[149,150] for the elements in the reactions considered here. SCF calculations and geometry optimizations by Gaussian 16 were conducted with tight convergence criteria. The DFT numerical integration grid had 175 radial shells per atom for H, 250 radial shells per atom for C and O, and 974 angular points per shell with pruning.

The OH spin−orbit splitting (140 cm^{-1}) was included in the reactant electronic PF.

5.2. CNEO Quantum Mechanical Treatment of H and D. In CNEO−DFT calculations, all hydrogen nuclei were treated quantum mechanically, and PB4F1 basis functions[151] were employed as nuclear basis functions, with no consideration for electron−proton correlation[128,152] or proton−proton correlation (or, for the deuterated cases, also no consideration of electron-deuteron, proton-deuteron, or deuteron−deuteron correlation) for most of the calculations, and only the epc17−2 electron−proton correlation functional[128] is used in the CH_4 + OH reaction. For nuclear basis functions centered on a deuteron, the exponents of the original PB4F1 basis functions were multiplied by $\sqrt{m_D/m_H}$. Calculations in PySCF used an SCF energy convergence threshold of 10^{-11} a.u., an SCF gradient convergence threshold of 10^{-7} a.u. and a geometry optimization gradient convergence threshold of 10^{-6} a.u.

5.3. Vibrational Scale Factors. No scaling is applied in any CNEO calculations. The scale factors for CTST and CVT/SCT were obtained as follows.

For CVT/SCT calculations on the reactions D + H_2 → DH + H and H + D_2 → HD + D, we applied the standard scale factors of 0.987 for CCSD(T)/aug-cc-pVTZ,[93] and we approximated the scale factor for MN15/MG3S by the MN15/aug-cc-pVTZ value[153] of 0.976. A standard scale factor of 0.973[93] was applied to M08-HX/MG3S-calculated frequencies.

To obtain SRP scale factors, HCDPT2 calculations were conducted with Gaussian 16 to assess the anharmonic scale factor λ^{Anh} for each transition structure conformer. This factor represents the ratio between the anharmonic ZPE and the harmonic ZPE; its product with the standard harmonic scale factor λ^{H} = 0.984[93] for M08-HX/MG3S yields the overall SRP scale factor. In HDCPT2 calculations, optimized geometries and second-order derivatives were obtained by M08-HX/MG3S, while higher-order numerical derivatives were from MPW1K[154]/MG3S. This choice is driven by the sensitivity of numerical derivatives of (hybrid-)meta-GGAs to DFT integration grids; hence, a (hybrid-)GGA is preferable for third and fourth derivatives in HDCPT2 calculations.[113] The calculated SRP scale factors are 0.952 for eclipsed $CH_4OH^{‡}$, 0.939 for staggered $CH_4OH^{‡}$, 0.983 for eclipsed $CD_4OH^{‡}$, and 0.964 for staggered $CD_4OH^{‡}$.

5.4. Dynamics. The reaction path was computed in mass-scaled coordinates[73] with a mass of 1 amu by employing the modified Page-McIver integrator[155,156] (in which the Hessian matrix is updated only every ninth step) and the reorientation of the dividing surface (RODS) algorithm.[157] The step size was set to 0.002 Å. For generalized normal-mode analyses along the reaction path, redundant curvilinear internal coordinates were employed.[75] For SCT calculations, we computed sufficiently long reaction paths to achieve convergence of the tunneling transmission coefficients.

In defining redundant internal coordinates, we treated the C−H−O angle as nonlinear, even though it is close to 180 deg (around 170°).

Transition structures for CH_4 + OH → CH_3 + H_2O and CD_4 + OH → CD_3 + HDO can have two possible conformers, namely eclipsed and staggered,[23,158] which are linked by the methyl torsion. Past studies using Hartree−Fock, MP-SAC2, and CCSD(T)-F12a identified the staggered conformer as the sole transition structure conformer with one imaginary frequency,[50,158] whereas MP2 calculations indicated the eclipsed conformer as the only transition structure conformer.[23] However, in contrast to both of the above scenarios, M08-HX and CNEO-M08-HX predict that both the eclipsed and the staggered conformers are transition structures, each with only one imaginary frequency, and that the eclipsed conformer is slightly lower in energy. To account for the multistructural torsional anharmonicity, we used the multi-structural method based on a coupled torsional potential [MS-T(C)][94,95] with a total of six of minima for the methyl torsion, including two distinguishable minima. Therefore, technically speaking, the calculations for these reactions are by multi-structural CVT/SCT (MS-CVT/SCT)[159] and multistructural CNEO-TST (MS-CNEO-TST).

A rotational symmetry number of 12 is applied in the CH_4 and CD_4 rotational PFs.

5.5. Software. In this study, CTST and CVT calculations are performed using Polyrate 17-C[160] and Gaussrate 17-B.[161] For DFT PES calculations, Gaussian 16[162] is called by Gaussrate as the calculator, and the SCT method[22,63] is used to compute tunneling transmission coefficients. The CNEO calculations employ CNEO−DFT,[79] and they were carried out with a locally modified version[163] of PySCF[164,165] by using Python scripts to establish a connection between Gaussrate and PySCF. To properly evaluate the combined electronic and vibrational PF when employing CNEO−DFT, modifications are made to the source code of Polyrate to prevent double counting of vibrational ZPE. CCSD(T)[104] calculations for the reactions D + H_2 → DH + H and H + D_2 → HD + D were conducted using Gaussian 16. Torsional anharmonicity was treated by using the MSTor 2023 code.[166]

■ ASSOCIATED CONTENT

Supporting Information

The Supporting Information is available free of charge at https://pubs.acs.org/doi/10.1021/acs.jctc.4c01521.

A Jupyter notebook containing data and Python code to generate all figures. Separate XYZ files provide geometries along the reaction coordinates for CH_4 + OH and CD_4 + OH reactions, used in Figures 5 and 7 (PDF)

Jupyter notebook and XYZ files are all in the zip files (ZIP)

■ AUTHOR INFORMATION

Corresponding Author

Yang Yang − *Theoretical Chemistry Institute and Department of Chemistry, University of Wisconsin−Madison, Madison, Wisconsin 53706, United States;* orcid.org/0000-0001-8572-5155; Email: yyang222@wisc.edu

https://doi.org/10.1021/acs.jctc.4c01521
J. Chem. Theory Comput. 2025, 21, 590−604

Authors

Zehua Chen − *Theoretical Chemistry Institute and Department of Chemistry, University of Wisconsin−Madison, Madison, Wisconsin 53706, United States;* orcid.org/0000-0002-1839-5034

Jingjing Zheng − *Gaussian, Inc., Wallingford, Connecticut 06492, United States*

Donald G. Truhlar − *Department of Chemistry, Chemical Theory Center, and Minnesota Supercomputing Institute, University of Minnesota, Minneapolis, Minnesota 55455, United States;* orcid.org/0000-0002-7742-7294

Complete contact information is available at: https://pubs.acs.org/10.1021/acs.jctc.4c01521

Notes

The authors declare no competing financial interest.

■ ACKNOWLEDGMENTS

The authors thank Tanner Culpitt for helpful discussions. Z.C. and Y.Y. are grateful for the funding support from the National Science Foundation under grant no. 2238473. D.G.T. acknowledges support from the U.S. Department of Energy, Office of Science, Office of Basic Energy Sciences under award DE-SC0015997. The authors thank the Center for High Throughput Computing at the University of Wisconsin−Madison for computational resource support.[167]

■ REFERENCES

(1) Roth, J. P.; Yoder, J. C.; Won, T.-J.; Mayer, J. M. Application of the Marcus Cross Relation to Hydrogen Atom Transfer Reactions. *Science* **2001**, *294*, 2524−2526.

(2) Sauer, J. Proton Transfer in Zeolites. *In Hydrogen-Transfer Reactions*; Hynes, J. T., Klinman, J. P., Limbach, H.-H., Schowen, R. L., Eds.; Wiley-VCH: Weinheim, Germany, 2007; Vol. 2, pp 685−707.

(3) Mayer, J. M. Understanding Hydrogen Atom Transfer: From Bond Strengths to Marcus Theory. *Acc. Chem. Res.* **2011**, *44*, 36−46.

(4) Lewis, J.; Coelho, P.; Arnold, F. Enzymatic Functionalization of Carbon−Hydrogen Bonds. *Chem. Soc. Rev.* **2011**, *40*, 2003−2021.

(5) Jin, J.; MacMillan, D. W. Alcohols as Alkylating Agents in Heteroarene C−H Functionalization. *Nature* **2015**, *525*, 87−90.

(6) Skubi, K. L.; Blum, T. R.; Yoon, T. P. Dual Catalysis Strategies in Photochemical Synthesis. *Chem. Rev.* **2016**, *116*, 10035−10074.

(7) Klinman, J. P.; Offenbacher, A. R. Understanding Biological Hydrogen Transfer Through the Lens of Temperature Dependent Kinetic Isotope Effects. *Acc. Chem. Res.* **2018**, *51*, 1966−1974.

(8) Kärkäs, M. D. Electrochemical Strategies for C−H Functionalization and C−N Bond Formation. *Chem. Soc. Rev.* **2018**, *47*, 5786−5865.

(9) Cao, H.; Tang, X.; Tang, H.; Yuan, Y.; Wu, J. Photoinduced Intermolecular Hydrogen Atom Transfer Reactions in Organic Synthesis. *Chem. Cat.* **2021**, *1*, 523−598.

(10) Jin, Y.; Zhang, Q.; Wang, L.; Wang, X.; Meng, C.; Duan, C. Convenient C(sp^3)−H Bond Functionalisation of Light Alkanes and Other Compounds by Iron Photocatalysis. *Green Chem.* **2021**, *23*, 6984−6989.

(11) Capaldo, L.; Ravelli, D.; Fagnoni, M. Direct Photocatalyzed Hydrogen Atom Transfer (HAT) for Aliphatic C−H Bonds Elaboration. *Chem. Rev.* **2022**, *122*, 1875−1924.

(12) Yang, C.; Arora, S.; Maldonado, S.; Pratt, D. A.; Stephenson, C. R. J. The Design of PINO-like Hydrogen-Atom-Transfer Catalysts. *Nat. Rev. Chem* **2023**, *7*, 653−666.

(13) Cernak, T.; Dykstra, K. D.; Tyagarajan, S.; Vachal, P.; Krska, S. W. The Medicinal Chemist's Toolbox for Late Stage Functionalization of Drug-Like Molecules. *Chem. Soc. Rev.* **2016**, *45*, 546−576.

(14) Farney, E. P.; Feng, S. S.; Schäfers, F.; Reisman, S. E. Total Synthesis of (+)-Pleuromutilin. *J. Am. Chem. Soc.* **2018**, *140*, 1267−1270.

(15) Correa, D. F.; Beyer, H. L.; Fargione, J. E.; Hill, J. D.; Possingham, H. P.; Thomas-Hall, S. R.; Schenk, P. M. Towards the Implementation of Sustainable Biofuel Production Systems. *Renew. Sustain. Energy Rev.* **2019**, *107*, 250−263.

(16) Eyring, H. The Activated Complex in Chemical Reactions. *J. Chem. Phys.* **1935**, *3*, 107−115.

(17) Truhlar, D. G.; Hase, W. L.; Hynes, J. T. Current Status of Transition-State Theory. *J. Phys. Chem.* **1983**, *87*, 2664−2682.

(18) Truhlar, D. G.; Garrett, B. C.; Klippenstein, S. J. Current Status of Transition-State Theory. *J. Phys. Chem.* **1996**, *100*, 12771−12800.

(19) Fernández-Ramos, A.; Miller, J. A.; Klippenstein, S. J.; Truhlar, D. G. Modeling the Kinetics of Bimolecular Reactions. *Chem. Rev.* **2006**, *106*, 4518−4584.

(20) Herschbach, D. R.; Johnston, H. S.; Pitzer, K.; Powell, R. Theoretical Pre-Exponential Factors for Twelve Bimolecular Reactions. *J. Chem. Phys.* **1956**, *25*, 736−741.

(21) Golden, D. M. Experimental and Theoretical Examples of the Value and Limitations of Transition State Theory. *J. Phys. Chem.* **1979**, *83*, 108−113.

(22) Liu, Y. P.; Lynch, G. C.; Truong, T. N.; Lu, D. H.; Truhlar, D. G.; Garrett, B. C. Molecular Modeling of the Kinetic Isotope Effect for the [1,5]-Sigmatropic Rearrangement of *cis*-1,3-Pentadiene. *J. Am. Chem. Soc.* **1993**, *115*, 2408−2415.

(23) Melissas, V. S.; Truhlar, D. G. Interpolated Variational Transition State Theory and Tunneling Calculations of the Rate Constant of the Reaction OH + CH_4 at 223−2400 K. *J. Chem. Phys.* **1993**, *99*, 1013−1027.

(24) Pu, J.; Truhlar, D. G. Parametrized Direct Dynamics Study of Rate Constants of H with CH_4 from 250 to 2400 K. *J. Chem. Phys.* **2002**, *116*, 1468−1478.

(25) Truhlar, D. G.; Garrett, B. C. Variational Transition State Theory in the Treatment of Hydrogen Transfer Reactions. In*Hydrogen-Transfer Reactions*; Hynes, J. T., Klinman, J. P., Limbach, H.-H., Schowen, R. L., Eds.; Wiley-VCH: Weinheim, Germany, 2007; Vol. 2, pp 833−874, .

(26) Ingold, K. U. Quantum Mechanical Tunneling of Hydrogen Atoms in Some Simple Chemical Systems.. In *Hydrogen-Transfer Reactions*; Hynes, J. T., Klinman, J. P., Limbach, H.-H., Schowen, R. L., Eds.; Wiley-VCH: Weinheim, Germany, 2007; Vol. 2, pp 875−893, .

(27) Meana-Pañeda, R.; Xu, X.; Ma, H.; Truhlar, D. G. Computational Kinetics by Variational Transition-State Theory with Semiclassical Multidimensional Tunneling: Direct Dynamics Rate Constants for the Abstraction of H from CH_3OH by Triplet Oxygen Atoms. *J. Phys. Chem. A* **2017**, *121*, 1693−1707.

(28) Klippenstein, S. J. Spiers Memorial Lecture: Theory of Unimolecular Reactions. *Faraday Discuss.* **2022**, *238*, 11−67.

(29) Zhao, Y.-C.; Long, B.; Francisco, J. S. Quantitative Kinetics of the Reaction between CH_2OO and H_2O_2 in the Atmosphere. *J. Phys. Chem. A* **2022**, *126*, 6742−6750.

(30) Olson, A.; Halford, R. The Rate and Mechanism of Hydrolysis and Alcoholysis of Tertiary Butyl Chloride. An Application to the Transition State Theory of Solvent Effects. *J. Am. Chem. Soc.* **1937**, *59*, 2644−2647.

(31) Lienhard, G. E. Enzymatic Catalysis and Transition-State Theory: Transition-State Analogs Show That Catalysis Is Due to Tighter Binding of Transition States Than of Substrates. *Science* **1973**, *180*, 149−154.

(32) Cui, Q.; Karplus, M. Quantum Mechanics/Molecular Mechanics Studies of Triosephosphate Isomerase-Catalyzed Reactions: Effect of Geometry and Tunneling on Proton-Transfer Rate Constants. *J. Am. Chem. Soc.* **2002**, *124*, 3093−3124.

(33) Truhlar, D. G.; Pliego, J. R. Transition State Theory and Chemical Reaction Dynamics in Solution. In *Continuum Solvation Models in Chemical Physics: From Theory to Applications*; Mennucci, B., Cammi, R., Eds.; Wiley: Chichester, 2008; pp 338−365.

(34) Kim, Y.; Mohrig, J. R.; Truhlar, D. G. Free-Energy Surfaces for Liquid-Phase Reactions and Their Use to Study the Border between Concerted and Nonconcerted α, β-Elimination Reactions of Esters and Thioesters. *J. Am. Chem. Soc.* **2010**, *132*, 11071−11082.
(35) Świderek, K.; Tuñón, I.; Martí, S.; Moliner, V. Protein Conformational Landscapes and Catalysis. Influence of Active Site Conformations in the Reaction Catalyzed by L-Lactate Dehydrogenase. *ACS Catal.* **2015**, *5*, 1172−1185.
(36) Schatz, G. C.; Kuppermann, A. Quantum Mechanical Reactive Scattering for Three-Dimensional Atom Plus Diatom Systems. I. Theory. *J. Chem. Phys.* **1976**, *65*, 4642−4667.
(37) Schatz, G. C.; Kuppermann, A. Quantum Mechanical Reactive Scattering for Three-Dimensional Atom Plus Diatom Systems. II. Accurate Cross Sections for H+H_2. *J. Chem. Phys.* **1976**, *65*, 4668−4692.
(38) Truhlar, D. G.; Schwenke, D. W.; Kouri, D. J. Quantum Dynamics of Chemical Reactions by Converged Algebraic Variational Calculations. *J. Phys. Chem.* **1990**, *94*, 7346−7352.
(39) Althorpe, S. C.; Clary, D. C. Quantum Scattering Calculations on Chemical Reactions. *Annu. Rev. Phys. Chem.* **2003**, *54*, 493−529.
(40) Wang, H.; Skinner, D. E.; Thoss, M. Calculation of Reactive Flux Correlation Functions for Systems in a Condensed Phase Environment: A Multilayer Multiconfiguration Time-Dependent Hartree Approach. *J. Chem. Phys.* **2006**, *125*, 174502.
(41) Karplus, M.; Porter, R. N.; Sharma, R. D. Dynamics of Reactive Collisions: The H + H_2 Exchange Reaction. *J. Chem. Phys.* **1964**, *40*, 2033−2034.
(42) Schatz, G. C.; Bowman, J. M.; Kuppermann, A. Exact Quantum, Quasiclassical, and Semiclassical Reaction Probabilities for the Collinear F+H_2 → FH+H Reaction. *J. Chem. Phys.* **1975**, *63*, 674−684.
(43) Lee, K. T.; Bowman, J. M.; Wagner, A. F.; Schatz, G. C. A Comparative Study of the Reaction Dynamics of Several Potential Energy Surfaces for O(^{3}P)+H_2 → OH+H. II. Collinear Exact Quantum and Quasiclassical Reaction Probabilities. *J. Chem. Phys.* **1982**, *76*, 3563−3582.
(44) Schatz, G. C. The Quantum Dynamics of H + H_2(ν = 1): A Coupled States Study of Cross Sections and Rate Constants. *Chem. Phys. Lett.* **1983**, *94*, 183−187.
(45) Schatz, G. C. The Origin of Cross Section Thresholds in H +H_2: Why Quantum Dynamics Appears to Be More Vibrationally Adiabatic than Classical Dynamics. *J. Chem. Phys.* **1983**, *79*, 5386−5391.
(46) Geva, E.; Shi, Q.; Voth, G. A. Quantum-Mechanical Reaction Rate Constants from Centroid Molecular Dynamics Simulations. *J. Chem. Phys.* **2001**, *115*, 9209−9222.
(47) Shi, Q.; Geva, E. Centroid-Based Methods for Calculating Quantum Reaction Rate Constants: Centroid Sampling versus Centroid Dynamics. *J. Chem. Phys.* **2002**, *116*, 3223−3233.
(48) Craig, I. R.; Manolopoulos, D. E. Chemical Reaction Rates from Ring Polymer Molecular Dynamics. *J. Chem. Phys.* **2005**, *122*, 084106.
(49) Craig, I. R.; Manolopoulos, D. E. A. A Refined Ring Polymer Molecular Dynamics Theory of Chemical Reaction Rates. *J. Chem. Phys.* **2005**, *123*, 034102.
(50) Li, J.; Guo, H. Thermal Rate Coefficients and Kinetic Isotope Effects for the Reaction OH + CH_4 → H_2O + CH_3 on an Ab Initio-Based Potential Energy Surface. *J. Phys. Chem. A* **2018**, *122*, 2645−2652.
(51) Liu, Y.; Li, J. An Accurate Potential Energy Surface and Ring Polymer Molecular Dynamics Study of the Cl + CH_4 → HCl + CH_3 Reaction. *Phys. Chem. Chem. Phys.* **2020**, *22*, 344−353.
(52) Li, X.; Huo, P. Investigating Tunneling-Controlled Chemical Reactions through Ab Initio Ring Polymer Molecular Dynamics. *J. Phys. Chem. Lett.* **2021**, *12*, 6714−6721.
(53) Gui, X.; Fan, W.; Sun, J.; Li, Y. New Stable and Fast Ring-Polymer Molecular Dynamics for Calculating Bimolecular Rate Coefficients with an Example of OH + CH_4. *J. Chem. Theory Comput.* **2022**, *18*, 5203−5212.
(54) Yamamoto, T. Quantum Statistical Mechanical Theory of the Rate of Exchange Chemical Reactions in the Gas Phase. *J. Chem. Phys.* **1960**, *33*, 281−289.
(55) Miller, W. H. Quantum Mechanical Transition State Theory and a New Semiclassical Model for Reaction Rate Constants. *J. Chem. Phys.* **1974**, *61*, 1823−1834.
(56) Miller, W. H.; Schwartz, S. D.; Tromp, J. W. Quantum Mechanical Rate Constants for Bimolecular Reactions. *J. Chem. Phys.* **1983**, *79*, 4889−4898.
(57) Miller, W. H. Semiclassical Limit of Quantum Mechanical Transition State Theory for Nonseparable Systems. *J. Chem. Phys.* **1975**, *62*, 1899−1906.
(58) Chapman, S.; Garrett, B. C.; Miller, W. H. Semiclassical Transition State Theory for Nonseparable Systems: Application to the Collinear H+H_2 Reaction. *J. Chem. Phys.* **1975**, *63*, 2710−2716.
(59) Voth, G. A.; Chandler, D.; Miller, W. H. Rigorous Formulation of Quantum Transition State Theory and Its Dynamical Corrections. *J. Chem. Phys.* **1989**, *91*, 7749−7760.
(60) Andersson, S.; Nyman, G.; Arnaldsson, A.; Manthe, U.; Jónsson, H. Comparison of Quantum Dynamics and Quantum Transition State Theory Estimates of the H + CH_4 Reaction Rate. *J. Phys. Chem. A* **2009**, *113*, 4468−4478.
(61) Truhlar, D. G.; Garrett, B. C. Variational Transition-State Theory. *Acc. Chem. Res.* **1980**, *13*, 440−448.
(62) Bao, J. L.; Truhlar, G. Variational Transition State Theory: Theoretical Framework and recent developments. *Chem. Soc. Rev.* **2017**, *46*, 7548−7596.
(63) Lu, D.-h.; Truong, T. N.; Melissas, V. S.; Lynch, G. C.; Liu, Y.-P.; Garrett, B. C.; Steckler, R.; Isaacson, A. D.; Rai, S. N.; Hancock, G. C.; Lauderdale, J. G.; Joseph, T.; Truhlar, D. G. POLYRATE 4: A New Version of a Computer Program for the Calculation of Chemical Reaction Rates for Polyatomics. *Comput. Phys. Commun.* **1992**, *71*, 235−262.
(64) Fernández-Ramos, A.; Truhlar, D. G. A New Algorithm for Efficient Direct Dynamics Calculations of Large-Curvature Tunneling and Its Application to Radical Reactions with 9−15 Atoms. *J. Chem. Theory Comput.* **2005**, *1*, 1063−1078.
(65) Allison, T. C.; Truhlar, D. G. Testing the Accuracy of Practical Semiclassical Methods: Variational Transition State Theory with Optimized Multidimensional Tunneling. In *Modern Methods for Multidimensional Dynamics Computations in Chemistry*; Thompson, D. L., Ed.; World Scientific: Singapore, 1998; pp 618−712.
(66) Pu, J.; Truhlar, D. G. Validation of Variational Transition State Theory with Multidimensional Tunneling Contributions Against Accurate Quantum Mechanical Dynamics for H+CH_4→ H_2+CH_3 in an Extended Temperature Interval. *J. Chem. Phys.* **2002**, *117*, 1479−1481.
(67) Mielke, S. L.; Peterson, K. A.; Schwenke, D. W.; Garrett, B. C.; Truhlar, D. G.; Michael, J. V.; Su, M.-C.; Sutherland, J. W. H + H_2 Thermal Reaction: A Convergence of Theory and Experiment. *Phys. Rev. Lett.* **2003**, *91*, 063201.
(68) Truhlar, D. G.; Gao, J.; Garcia-Viloca, M.; Alhambra, C.; Corchado, J.; Sanchez, M. L.; Poulsen, T. D. Ensemble-Averaged Variational Transition State Theory with Optimized Multidimensional Tunneling for Enzyme Kinetics and Other Condensed-Phase Reactions. *Int. J. Quantum Chem.* **2004**, *100*, 1136−1152.
(69) Fleming, D. G.; Arseneau, D. J.; Sukhorukov, O.; Brewer, J. H.; Mielke, S. L.; Schatz, G. C.; Garrett, B. C.; Peterson, K. A.; Truhlar, D. G. Kinetic Isotope Effects for the Reactions of Muonic Helium and Muonium with H_2. *Science* **2011**, *331*, 448−450.
(70) Long, B.; Bao, J. L.; Truhlar, D. G. Kinetics of the Strongly Correlated CH_3O + O_2 Reaction: The Importance of Quadruple Excitations in Atmospheric and Combustion Chemistry. *J. Am. Chem. Soc.* **2019**, *141*, 611−617.
(71) Xing, L.; Lian, L.; Wang, Z.; Cheng, Z.; He, Y.; Cui, J.; Truhlar, D. G. Lowering of Reaction Rates by Energetically Favorable Hydrogen Bonding in the Transition State. Degradation of Biofuel Ketohydroperoxides by OH. *J. Am. Chem. Soc.* **2022**, *144*, 16984−16995.

https://doi.org/10.1021/acs.jctc.4c01521
J. Chem. Theory Comput. 2025, 21, 590−604

(72) Long, B.; Xia, Y.; Truhlar, D. G. Quantitative Kinetics of HO_2 Reactions with Aldehydes in the Atmosphere: High-Order Dynamic Correlation, Anharmonicity, and Falloff Effects Are All Important. *J. Am. Chem. Soc.* **2022**, *144*, 19910−19920.
(73) Isaacson, A. D.; Truhlar, D. G. Polyatomic Canonical Variational Theory for Chemical Reaction Rates. Separable-Mode Formalism with Application to $OH+H_2 \rightarrow H_2O+H$. *J. Chem. Phys.* **1982**, *76*, 1380−1391.
(74) Jackels, C. F.; Gu, Z.; Truhlar, D. G. Reaction-Path Potential and Vibrational Frequencies in Terms of Curvilinear Internal Coordinates. *J. Chem. Phys.* **1995**, *102*, 3188−3201.
(75) Chuang, Y.-Y.; Truhlar, D. G. Reaction-Path Dynamics in Redundant Internal Coordinates. *J. Phys. Chem. A* **1998**, *102*, 242−247.
(76) Mahan, B. H. Activated Complex Theory of Bimolecular Reactions. *J. Chem.* **1974**, *51*, 709−711.
(77) Born, M. Kopplung der Elektronen- und Kernbewegung in Molekeln und Kristallen. *Nachr. Akad. Wiss. Göttingen* **1951**, *6*, 1−3.
(78) Pavošević, F.; Culpitt, T.; Hammes-Schiffer, S. Multicomponent Quantum Chemistry: Integrating Electronic and Nuclear Quantum Effects via the Nuclear−Electronic Orbital Method. *Chem. Rev.* **2020**, *120*, 4222−4253.
(79) Xu, X.; Yang, Y. Constrained Nuclear-Electronic Orbital Density Functional Theory: Energy Surfaces with Nuclear Quantum Effects. *J. Chem. Phys.* **2020**, *152*, 084107.
(80) Zhao, L.; Tao, Z.; Pavošević, F.; Wildman, A.; Hammes-Schiffer, S.; Li, X. Real-Time Time-Dependent Nuclear-Electronic Orbital Approach: Dynamics Beyond the Born−Oppenheimer Approximation. *J. Phys. Chem. Lett.* **2020**, *11*, 4052−4058.
(81) Zhao, L.; Wildman, A.; Tao, Z.; Schneider, P.; Hammes-Schiffer, S.; Li, X. Nuclear−Electronic Orbital Ehrenfest Dynamics. *J. Chem. Phys.* **2020**, *153*, 224111−224119.
(82) Xu, X.; Yang, Y. Full-Quantum Descriptions of Molecular Systems from Constrained Nuclear−Electronic Orbital Density Functional Theory. *J. Chem. Phys.* **2020**, *153*, 074106.
(83) Xu, X.; Yang, Y. Molecular Vibrational Frequencies from Analytic Hessian of Constrained Nuclear−Electronic Orbital Density Functional Theory. *J. Chem. Phys.* **2021**, *154*, 244110.
(84) Chen, Z.; Yang, Y. Incorporating Nuclear Quantum Effects in Molecular Dynamics with a Constrained Minimized Energy Surface. *J. Phys. Chem. Lett.* **2023**, *14*, 279−286.
(85) Wang, Y.; Chen, Z.; Yang, Y. Calculating Vibrational Excited State Absorptions with Excited State Constrained Minimized Energy Surfaces. *J. Phys. Chem. A* **2023**, *127*, 5491−5501.
(86) Gonzalez-Lafont, A.; Truong, T. N.; Truhlar, D. G. Direct Dynamics Calculations with NDDO (Neglect of Diatomic Differential Overlap) Molecular Orbital Theory with Specific Reaction Parameters. *J. Phys. Chem.* **1991**, *95*, 4618−4627.
(87) Bartlett, R. J.; Musiał, M. Coupled-Cluster Theory in Quantum Chemistry. *Rev. Mod. Phys.* **2007**, *79*, 291−352.
(88) Zhao, Y.; Truhlar, D. G. Exploring the Limit of Accuracy of the Global Hybrid Meta Density Functional for Main-Group Thermochemistry, Kinetics, and Noncovalent Interactions. *J. Chem. Theory Comput.* **2008**, *4*, 1849−1868.
(89) Yu, H. S.; He, X.; Li, S. L.; Truhlar, D. G. MN15: A Kohn−Sham Global-Hybrid Exchange−Correlation Density Functional with Broad Accuracy for Multi-Reference and Single-Reference Systems and Noncovalent Interactions. *Chem. Sci.* **2016**, *7*, 5032−5051.
(90) Kohn, W.; Sham, L. J. Self-Consistent Equations Including Exchange and Correlation Effects. *Phys. Rev.* **1965**, *140*, A1133−A1138.
(91) Laidler, K. J. *Chemical Kinetics*, 3rd ed.; Prentice-Hall, 1987; Chapter 5.
(92) Eyring, H. The Theory of Absolute Reaction Rates. *Trans. Faraday Soc.* **1938**, *34*, 41−48.
(93) Alecu, I. M.; Zheng, J.; Zhao, Y.; Truhlar, D. G. Computational Thermochemistry: Scale Factor Databases and Scale Factors for Vibrational Frequencies Obtained from Electronic Model Chemistries. *J. Chem. Theory Comput.* **2010**, *6*, 2872−2887.
(94) Zheng, J.; Yu, T.; Papajak, E.; Alecu, I. M.; Mielke, S. L.; Truhlar, D. G. Practical Methods for Including Torsional Anharmonicity in Thermochemical Calculations on Complex Molecules: The Internal-Coordinate Multi-Structural Approximation. *Phys. Chem. Chem. Phys.* **2011**, *13*, 10885−10907.
(95) Zheng, J.; Truhlar, D. G. Quantum Thermochemistry: Multistructural Method with Torsional Anharmonicity Based on a Coupled Torsional Potential. *J. Chem. Theory Comput.* **2013**, *9*, 1356−1367.
(96) Garrett, B. C.; Truhlar, D. G. Generalized Transition State Theory. Bond Energy-Bond Order Method for Canonical Variational Calculations with Application to Hydrogen Atom Transfer Reactions. *J. Am. Chem. Soc.* **1979**, *101*, 4534−4548.
(97) Xu, X.; Chen, Z.; Yang, Y. Molecular Dynamics with Constrained Nuclear Electronic Orbital Density Functional Theory: Accurate Vibrational Spectra from Efficient Incorporation of Nuclear Quantum Effects. *J. Am. Chem. Soc.* **2022**, *144*, 4039−4046.
(98) Zhang, Y.; Xu, X.; Yang, N.; Chen, Z.; Yang, Y. Describing Proton Transfer Modes in Shared Proton Systems with Constrained Nuclear−Electronic Orbital Methods. *J. Chem. Phys.* **2023**, *158*, 231101.
(99) Zhang, Y.; Wang, Y.; Xu, X.; Chen, Z.; Yang, Y. Vibrational Spectra of Highly Anharmonic Water Clusters: Molecular Dynamics and Harmonic Analysis Revisited with Constrained Nuclear-Electronic Orbital Methods. *J. Chem. Theory Comput.* **2023**, *19*, 9358−9368.
(100) Garrett, B. C.; Truhlar, D. G. Generalized Transition State Theory Calculations for the Reactions $D+H_2$ and $H + D_2$ using an Accurate Potential Energy Surface: Explanation of the Kinetic Isotope Effect. *J. Chem. Phys.* **1980**, *72*, 3460−3471.
(101) Ridley, B. A.; Schulz, W. R.; Le Roy, D. J. Kinetics of the Reaction $D+H_2=HD+H$. *J. Chem. Phys.* **1966**, *44*, 3344−3347.
(102) Westenberg, A. A.; de Haas, N. Atom—Molecule Kinetics Using ESR Detection. II. Results for $D + H_2 \rightarrow HD + H$ and $H + D_2 \rightarrow HD + D$. *J. Chem. Phys.* **1967**, *47*, 1393−1405.
(103) Mitchell, D. N.; Roy, D. J. L. Rate Constants for the Reaction $D + H_2 = DH + H$ at Low Temperatures Using ESR Detection. *J. Chem. Phys.* **1973**, *58*, 3449−3453.
(104) Raghavachari, K.; Trucks, G. W.; Pople, J. A.; Head-Gordon, M. A. Fifth-Order Perturbation Comparison of Electron Correlation Theories. *Chem. Phys. Lett.* **1989**, *157*, 479−483.
(105) Schulz, W. R.; Roy, D. J. L. Kinetics of the Reaction $H+D_2=HD+D$. *Can. J. Chem.* **1964**, *42*, 2480−2487.
(106) Jayaweera, I. S.; Pacey, P. D. Electron Spin Resonance Study of the Reaction of Hydrogen Atom with Deuterium at 274−364 K. *J. Phys. Chem.* **1990**, *94*, 3614−3620.
(107) Srinivasan, N. K.; Su, M.-C.; Sutherland, J. W.; Michael, J. V. Reflected Shock Tube Studies of High-Temperature Rate Constants for $OH + CH_4 \rightarrow CH_3 + H_2O$ and $CH_3 + NO_2 \rightarrow CH_3O + NO$. *J. Phys. Chem. A* **2005**, *109*, 1857−1863.
(108) Lynch, B. J.; Zhao, Y.; Truhlar, D. G. Effectiveness of Diffuse Basis Functions for Calculating Relative Energies by Density Functional Theory. *J. Phys. Chem. A* **2003**, *107*, 1384−1388.
(109) Zheng, J.; Zhao, Y.; Truhlar, D. G. The DBH24/08 Database and Its Use to Assess Electronic Structure Model Chemistries for Chemical Reaction Barrier Heights. *J. Chem. Theory Comput.* **2009**, *5*, 808−821.
(110) Hydrogen Transfers Barrier Heights. https://comp.chem.umn.edu/db/dbs/htbh38.html (accessed Jan 15, 2024).
(111) Mardirossian, N.; Head-Gordon, M. Thirty Years of Density Functional Theory in Computational Chemistry: An Overview and Extensive Assessment of 200 Density Functionals. *Mol. Phys.* **2017**, *115*, 2315−2372.
(112) Li, J.; Guo, H. Communication: An Accurate Full 15 Dimensional Permutationally Invariant Potential Energy Surface for the $OH + CH_4 \rightarrow H_2O + CH_3$ Reaction. *J. Chem. Phys.* **2015**, *143*, 221103.
(113) Zheng, J.; Meana-Pañeda, R.; Truhlar, D. G. Prediction of Experimentally Unavailable Product Branching Ratios for Biofuel

Combustion: The Role of Anharmonicity in the Reaction of Isobutanol with OH. *J. Am. Chem. Soc.* **2014**, *136*, 5150−5160.
(114) Zheng, J.; Oyedepo, G. A.; Truhlar, D. G. Kinetics of the Hydrogen Abstraction Reaction from 2-Butanol by OH Radical. *J. Phys. Chem. A* **2015**, *119*, 12182−12192.
(115) Bao, J. L.; Zheng, J.; Truhlar, D. G. Kinetics of Hydrogen Radical Reactions with Toluene Including Chemical Activation Theory Employing System-Specific Quantum RRK Theory Calibrated by Variational Transition State Theory. *J. Am. Chem. Soc.* **2016**, *138*, 2690−2704.
(116) Zhang, H.; Zhang, X.; Truhlar, D. G.; Xu, X. Nonmonotonic Temperature Dependence of the Pressure-Dependent Reaction Rate Constant and Kinetic Isotope Effect of Hydrogen Radical Reaction with Benzene Calculated by Variational Transition-State Theory. *J. Phys. Chem. A* **2017**, *121*, 9033−9044.
(117) Gao, L. G.; Zheng, J.; Fernández-Ramos, A.; Truhlar, D. G.; Xu, X. Kinetics of the Methanol Reaction with OH at Interstellar, Atmospheric, and Combustion Temperatures. *J. Am. Chem. Soc.* **2018**, *140*, 2906−2918.
(118) Wu, J.; Gao, L. G.; Varga, Z.; Xu, X.; Ren, W.; Truhlar, D. G. Water Catalysis of the Reaction of Methanol with OH Radical in the Atmosphere is Negligible. *Angew. Chem., Int. Ed.* **2020**, *59*, 10826−10830.
(119) Gao, L. G.; Fleming, D. G.; Truhlar, D. G.; Xu, X. Large Anharmonic Effects on Tunneling and Kinetics: Reaction of Propane with Muonium. *J. Phys. Chem. Lett.* **2021**, *12*, 4154−4159.
(120) Sun, Y.; Long, B.; Truhlar, D. G. Unimolecular Reactions of E-Glycolaldehyde Oxide and Its Reactions with One and Two Water Molecules. *Research* **2023**, *6*, 0143.
(121) Long, B.; Xia, Y.; Zhang, Y.-Q.; Truhlar, D. G. Kinetics of Sulfur Trioxide Reaction with Water Vapor to Form Atmospheric Sulfuric Acid. *J. Am. Chem. Soc.* **2023**, *145*, 19866−19876.
(122) *Atoms III-Molecules I/Atome III*; Nielsen, H.; Moleküle, I.; Flügge, S., Eds.; Springer Berlin, 1959; Chapter The Vibration-Rotation Energies of Molecules and Their Spectra in the Infra-Red, pp 173−313.
(123) Truhlar, D. G.; Isaacson, A. D. Simple Perturbation Theory Estimates of Equilibrium Constants from Force Fields. *J. Chem. Phys.* **1991**, *94*, 357−359.
(124) Kuhler, K. M.; Truhlar, D. G.; Isaacson, A. D. General Method for Removing Resonance Singularities in Quantum Mechanical Perturbation Theory. *J. Chem. Phys.* **1996**, *104*, 4664−4671.
(125) Bloino, J.; Barone, V. A Second-Order Perturbation Theory Route to Vibrational Averages and Transition Properties of Molecules: General Formulation and Application to Infrared and Vibrational Circular Dichroism Spectroscopies. *J. Chem. Phys.* **2012**, *136*, 124108.
(126) Ramírez, R.; López-Ciudad, T.; Noya, J. C. Feynman Effective Classical Potential in the Schrödinger Formulation. *Phys. Rev. Lett.* **1998**, *81*, 3303−3306.
(127) Ramírez, R.; López-Ciudad, T. The Schrödinger Formulation of the Feynman Path Centroid Density. *J. Chem. Phys.* **1999**, *111*, 3339−3348.
(128) Brorsen, K. R.; Yang, Y.; Hammes-Schiffer, S. Multicomponent Density Functional Theory: Impact of Nuclear Quantum Effects on Proton Affinities and Geometries. *J. Phys. Chem. Lett.* **2017**, *8*, 3488−3493.
(129) Yang, Y.; Zhang, Y.; Yang, Y.; Xu, X. Assessment of Electron-Proton Correlation Functionals for Vibrational Spectra of Shared-Proton Systems by Constrained Nuclear-Electronic Orbital Density Functional Theory. *J. Chem. Phys.* **2024**, *161*, 244103.
(130) Dunlop, J. R.; Tully, F. P. A Kinetic Study of Hydroxyl Radical Reactions with Methane and Perdeuterated Methane. *J. Phys. Chem.* **1993**, *97*, 11148−11150.
(131) Gierczak, T.; Talukdar, R. K.; Herndon, S. C.; Vaghjiani, G. L.; Ravishankara, A. R. Rate Coefficients for the Reactions of Hydroxyl Radicals with Methane and Deuterated Methanes. *J. Phys. Chem. A* **1997**, *101*, 3125−3134.
(132) Garrett, B. C.; Truhlar, D. G.; Magnuson, A. W. New Semiempirical Method of Modeling Potential Energy Surfaces for Generalized TST and Application to the Kinetic Isotope Effects in the Cl−H−H System. *J. Chem. Phys.* **1982**, *76*, 2321−2331.
(133) Tucker, S. C.; Truhlar, D. G.; Garrett, B. C.; Isaacson, A. D. Variational Transition State Theory with Least-Action Tunneling Calculations for the Kinetic Isotope Effects in the Cl+H_2 Reaction: Tests of Extended-LEPS, Information-Theoretic, and Diatomics-in-Molecules Potential Energy Surfaces. *J. Chem. Phys.* **1985**, *82*, 4102−4119.
(134) Garrett, B. C.; Truhlar, D. G.; Bowman, J. M.; Wagner, A. F. Evaluation of Dynamical Approximations for Calculating the Effect of Vibrational Excitation on Reaction Rates. O+ H_2 (n = 0, 1) → OH (n = 0, 1)+ H. *J. Phys. Chem.* **1986**, *90*, 4305−4311.
(135) Lu, D.-h.; Maurice, D.; Truhlar, D. G. What Is the Effect of Variational Optimization of the Transition State on α-Deuterium Secondary Kinetic Isotope Effects? A Prototype: CD_3H+ H → CD_3+ H_2. *J. Am. Chem. Soc.* **1990**, *112*, 6206−6214.
(136) Liu, Y.-P.; Lu, D.-h.; Gonzalez-Lafont, A.; Truhlar, D. G.; Garrett, B. C. Direct Dynamics Calculation of the Kinetic Isotope Effect for an Organic Hydrogen-Transfer Reaction, Including Corner-Cutting Tunneling in 21 Dimensions. *J. Am. Chem. Soc.* **1993**, *115*, 7806−7817.
(137) Lynch, G. C.; Truhlar, D. G.; Brown, F. B.; Zhao, J.-g. A New Potential Energy Surface for H_2Br and Its Use to Calculate Branching Ratios and Kinetic Isotope Effects for the H+HBr Reaction. *J. Phys. Chem.* **1995**, *99*, 207−225.
(138) Chakraborty, A.; Zhao, Y.; Lin, H.; Truhlar, D. G. Combined Valence Bond-Molecular Mechanics Potential-Energy Surface and Direct Dynamics Study of Rate Constants and Kinetic Isotope Effects for the H+C_2H_6 Reaction. *J. Chem. Phys.* **2006**, *124*, 044315.
(139) Meana-Pañeda, R.; Truhlar, D. G.; Fernández-Ramos, A. High-Level Direct-Dynamics Variational Transition State Theory Calculations Including Multidimensional Tunneling of the Thermal Rate Constants, Branching Ratios, and Kinetic Isotope Effects of the Hydrogen Abstraction Reactions from Methanol by Atomic Hydrogen. *J. Chem. Phys.* **2011**, *134*, 094302.
(140) Truhlar, D. G.; Kuppermann, A. Exact Tunneling Calculations. *J. Am. Chem. Soc.* **1971**, *93*, 1840−1851.
(141) Tolman, R. C. Statistical Merchanics Applied to Chemical Kinetics. *J. Am. Chem. Soc.* **1920**, *42*, 2506−2528.
(142) Truhlar, D. G. Interpretation of the Activation Energy. *J. Chem. Educ.* **1978**, *55*, 309−311.
(143) Marenich, A. V.; Cramer, C. J.; Truhlar, D. G. Universal Solvation Model Based on Solute Electron Density and on a Continuum Model of the Solvent Defined by the Bulk Dielectric Constant and Atomic Surface Tensions. *J. Phys. Chem. B* **2009**, *113*, 6378−6396.
(144) Marenich, A. V.; Cramer, C. J.; Truhlar, D. G. Generalized Born Solvation Model SM12. *J. Chem. Theory Comput.* **2013**, *9*, 609−620.
(145) *Continuum Solvation Models in Chemical Physics: From Theory to Applications*; Mennucci, B., Cammi, R., Eds.; Wiley: Chichester, 2008; pp 338−365.
(146) Zhao, X.; Chen, Z.; Yang, Y. Constrained Nuclear-Electronic Orbital QM/MM Approach for Simulating Complex Systems with Quantum Nuclear Delocalization Effects Incorporated. *Chem. Phys. Rev.* **2024**, *5*, 041401.
(147) Xu, X. Constrained Nuclear-Electronic Orbital Density Functional Theory with a Dielectric Continuum Solvent Model. *J. Phys. Chem. A* **2023**, *127*, 6329−6334.
(148) Kendall, R. A.; Dunning, T. H., Jr; Harrison, R. J. Electron Affinities of the First-Row Atoms Revisited. Systematic Basis Sets and Wave Functions. *J. Chem. Phys.* **1992**, *96*, 6796−6806.
(149) Krishnan, R.; Binkley, J. S.; Seeger, R.; Pople, J. A. Self-Consistent Molecular Orbital Methods. XX. A Basis Set for Correlated Wave Functions. *J. Chem. Phys.* **1980**, *72*, 650−654.

https://doi.org/10.1021/acs.jctc.4c01521
J. Chem. Theory Comput. 2025, 21, 590−604

(150) Frisch, M. J.; Pople, J. A.; Binkley, J. S. Self-Consistent Molecular Orbital Methods 25. supplementary Functions for Gaussian Basis Sets. *J. Chem. Phys.* **1984**, *80*, 3265−3269.
(151) Yu, Q.; Pavošević, F.; Hammes-Schiffer, S. Development of Nuclear Basis Sets for Multicomponent Quantum Chemistry Methods. *J. Chem. Phys.* **2020**, *152*, 244123.
(152) Yang, Y.; Brorsen, K. R.; Culpitt, T.; Pak, M. V.; Hammes-Schiffer, S. Development of a Practical Multicomponent Density Functional for Electron-Proton Correlation to Produce Accurate Proton Densities. *J. Chem. Phys.* **2017**, *147*, 114113−114117.
(153) Kanchanakungwankul, S.; Zheng, J.; Alecu, I. M.; Lynch, B. J.; Zhao, Y.; Truhlar, D. G. Database of Frequency Scale Factors for Electronic Model Chemistries, version 5. https://comp.chem.umn.edu/freqscale/ (accessed Jan 15, 2024).
(154) Lynch, B. J.; Fast, P. L.; Harris, M.; Truhlar, D. G. Adiabatic Connection for Kinetics. *J. Phys. Chem. A* **2000**, *104*, 4811−4815.
(155) Page, M.; McIver, J. W. On Evaluating the Reaction Path Hamiltonian. *J. Chem. Phys.* **1988**, *88*, 922−935.
(156) Melissas, V. S.; Truhlar, D. G.; Garrett, B. C. Optimized Calculations of Reaction Paths and Reaction-Path Functions for Chemical Reactions. *J. Chem. Phys.* **1992**, *96*, 5758−5772.
(157) Villa, J.; Truhlar, D. G. Variational Transition State Theory without the Minimum-Energy Path. *Theor. Chem. Acc.* **1997**, *97*, 317−323.
(158) Truong, T. N.; Truhlar, D. G. Ab Initio Transition State Theory Calculations of the Reaction Rate for $OH+CH_4 \rightarrow H_2O+CH_3$. *J. Chem. Phys.* **1990**, *93*, 1761−1769.
(159) Yu, T.; Zheng, J.; Truhlar, D. G. Multi-Structural Variational Transition State Theory. Kinetics of the 1, 4-Hydrogen Shift Isomerization of the Pentyl Radical with Torsional Anharmonicity. *Chem. Sci.* **2011**, *2*, 2199−2213.
(160) Zheng, J.; Bao, J. L.; Meana-Pañeda, R.; Zhang, S.; Lynch, B. J.; Corchado, J. C.; Chuang, Y.-Y.; Fast, P. L.; Hu, W.-P.; Liu, Y.-P.; Lynch, G. C.; Nguyen, K. A.; Jackels, C. F.; Fernandez Ramos, A.; Ellingson, B. A.; Melissas, V. S.; Villà, I.; Rossi, J.; Coitiño, E. L.; Pu, J.; Albu, T. V.; Ratkiewicz, A.; Steckler, R.; Garrett, B. C.; Isaacson, A. D.; Truhlar, D. G. *Polyrate*. version 2017-C; University of Minnesota: Minneapolis, 2017.
(161) Zheng, J.; Bao, J. L.; Zhang, S.; Corchado, J. C.; Meana-Pañeda, R.; Chuang, Y.-Y.; Coitiño, E. L.; Ellingson, B. A.; Truhlar, D. G. *Gaussrate 17*; University of Minnesota: Minneapolis, 2017.
(162) Frisch, M. J.; Trucks, G. W.; Schlegel, H. B.; Scuseria, G. E.; Robb, M. A.; Cheeseman, J. R.; Scalmani, G.; Barone, V.; Petersson, G. A.; Nakatsuji, H.; Li, X.; Caricato, M.; Marenich, A. V.; Bloino, J.; Janesko, B. G.; Gomperts, R.; Mennucci, B.; Hratchian, H. P.; Ortiz, J. V.; Izmaylov, A. F.; Sonnenberg, J. L.; Williams-Young, D.; Ding, F.; Lipparini, F.; Egidi, F.; Goings, J.; Peng, B.; Petrone, A.; Henderson, T.; Ranasinghe, D.; Zakrzewski, V. G.; Gao, J.; Rega, N.; Zheng, G.; Liang, W.; Hada, M.; Ehara, M.; Toyota, K.; Fukuda, R.; Hasegawa, J.; Ishida, M.; Nakajima, T.; Honda, Y.; Kitao, O.; Nakai, H.; Vreven, T.; Throssell, K.; Montgomery, J. A.; Peralta, J. E.; Ogliaro, F.; Bearpark, M. J.; Heyd, J. J.; Brothers, E. N.; Kudin, K. N.; Staroverov, V. N.; Keith, T. A.; Kobayashi, R.; Normand, J.; Raghavachari, K.; Rendell, A. P.; Burant, J. C.; Iyengar, S. S.; Tomasi, J.; Cossi, M.; Millam, J. M.; Klene, M.; Adamo, C.; Cammi, R.; Ochterski, J. W.; Martin, R. L.; Morokuma, K.; Farkas, O.; Foresman, J. B.; Fox, D. J. *Gaussian 16*. Revision C.01.; Gaussian Inc.: Wallingford CT, 2016.
(163) PySCF with CNEO Functionalities Implemented. https://github.com/theorychemyang/pyscf (accessed Jan 15, 2024).
(164) Sun, Q.; Berkelbach, T. C.; Blunt, N. S.; Booth, G. H.; Guo, S.; Li, Z.; Liu, J.; McClain, J. D.; Sayfutyarova, E. R.; Sharma, S.; Wouters, S.; Chan, G. K.-L. PyS. C. F. PySCF: The Python-based Simulations of Chemistry Framework. *Wiley Interdiscip. Rev. Comput. Mol. Sci.* **2018**, *8*, No. e1340.
(165) Sun, Q.; Zhang, X.; Banerjee, S.; Bao, P.; Barbry, M.; Blunt, N. S.; Bogdanov, N. A.; Booth, G. H.; Chen, J.; Cui, Z.-H.; Eriksen, J. J.; Gao, Y.; Guo, S.; Hermann, J.; Hermes, M. R.; Koh, K.; Koval, P.; Lehtola, S.; Li, Z.; Liu, J.; Mardirossian, N.; McClain, J. D.; Motta, M.; Mussard, B.; Pham, H. Q.; Pulkin, A.; Purwanto, W.; Robinson, P. J.; Ronca, E.; Sayfutyarova, E. R.; Scheurer, M.; Schurkus, H. F.; Smith, J. E. T.; Sun, C.; Sun, S.-N.; Upadhyay, S.; Wagner, L. K.; Wang, X.; White, A.; Whitfield, J. D.; Williamson, M. J.; Wouters, S.; Yang, J.; Yu, J. M.; Zhu, T.; Berkelbach, T. C.; Sharma, S.; Sokolov, A. Y.; Chan, G. K.-L. Recent Developments in the PySCF Program Package. *J. Chem. Phys.* **2020**, *153*, 024109.
(166) Chen, W.; Zheng, J.; Bao, J. L.; Truhlar, D. G.; Xu, X. MSTor 2023: A New Version of the Computer Code for Multistructural Torsional Anharmonicity, Now with Automatic Torsional Identification Using Redundant Internal Coordinates. *Comput. Phys. Commun.* **2023**, *288*, 108740.
(167) Center for High Throughput Computing Center for High Throughput Computing, 2006. https://chtc.cs.wisc.edu/ (accessed Dec 17, 2024).

https://doi.org/10.1021/acs.jctc.4c01521
J. Chem. Theory Comput. 2025, 21, 590−604